Atmos. Chem. Phys. Discuss., 11, 9887–9957, 2011
www.atmos-chem-phys-discuss.net/11/9887/2011/
doi:10.5194/acpd-11-9887-2011

Atmospheric Chemistry and Physics Discussions

Detailed comparisons of airborne formaldehyde measurements with box models during the 2006 INTEX-B campaign: potential evidence for unmeasured and multi-generation volatile organic carbon oxidation processing

A. Fried[1], C. Cantrell[2], J. Olson[3], J. H. Crawford[3], P. Weibring[1], J. Walega[1], D. Richter[1], W. Junkermann[4], R. Volkamer[5], R. Sinreich[5], B. G. Heikes[6], D. O'Sullivan[7], D. R. Blake[8], N. Blake[8], S. Meinardi[8], E. Apel[2], A. Weinheimer[2], D. Knapp[2], A. Perring[9], R. C. Cohen[9], H. Fuelberg[10], R. E. Shetter[2], S. R. Hall[2], K. Ullmann[2], W. H. Brune[11], J. Mao[12], X. Ren[13], L. G. Huey[14], H. B. Singh[15], J. W Hair[16], and D. Riemer[13]

[1]The National Center for Atmospheric Research, Earth Observing Laboratory, 3450 Mitchell Lane, Boulder, CO, USA

[2] The National Center for Atmospheric Research, Atmospheric Chemistry Division, 3450 Mitchell Lane, Boulder, CO, USA
[3] NASA Langley Research Center, Hampton, VA, USA
[4] Karlsruhe Institute of Technology, IMK-IFU, Garmisch-Partenkirchen, Germany
[5] The University of Colorado, Dept. of Chemistry, Boulder, CO, USA
[6] The University of Rhode Island, Narragansett, RI, USA
[7] United States Naval Academy, Annapolis, MD, USA
[8] University of California, Irvine, Irvine, CA, USA
[9] University of California, Berkeley, Berkley, CA, USA
[10] Florida State University, Tallahassee, Florida, USA
[11] Pennsylvania State University, University Park, PA, USA
[12] Harvard University, Cambridge, MA, USA
[13] University of Miami, Miami, FI, USA
[14] Georgia Institute of Technology, Atlanta, GA, USA
[15] NASA Ames Research, Moffett Field CA, USA
[16] NASA Lidar Applications Group, Langley Research Center, Hampton, VA, USA

Received: 8 March 2011 – Accepted: 15 March 2011 – Published: 24 March 2011

Correspondence to: A. Fried (fried@ucar.edu)

Published by Copernicus Publications on behalf of the European Geosciences Union.

ACPD
11, 9887–9957, 2011

Abstract

Detailed comparisons of airborne CH_2O measurements acquired by tunable diode laser absorption spectroscopy with steady state box model calculations were carried out using data from the 2006 INTEX-B campaign in order to improve our understanding of hydrocarbon oxidation processing. Select previous comparisons in other campaigns have highlighted some locations in the boundary layer where steady state box models have tended to underpredict CH_2O, suggesting that standard steady state modeling assumptions might be unsuitable under these conditions, and pointing to a possible role for unmeasured hydrocarbons and/or additional primary emission sources of CH_2O. Employing an improved instrument, more detailed measurement-model comparisons with better temporal overlap, up to date measurement and model precision estimates, up to date rate constants, and additional modeling tools based on both Lagrangian and Master Chemical Mechanism (MCM) runs, we have explained much of the disagreement between observed and predicted CH_2O as resulting from non-steady-state atmospheric conditions in the vicinity of large pollution sources, and have quantified the disagreement as a function of plume lifetime (processing time). We show that in the near-field (within ~4 to 6 h of the source), steady-state models can either over- or-underestimate observations, depending on the predominant non-steady-state influence. In addition, we show that even far field processes (10–40 h) can be influenced by non-steady-state conditions which can be responsible for CH_2O model underestimations by as much as a factor of 2. At the longer processing times in the 10 to 40 h range during Mexico City outflow events, MCM model calculations, using assumptions about emissions of high-order NMHCs, further indicate the potential importance of CH_2O produced from unmeasured and multi-generation hydrocarbon oxidation processing, particularly methylglyoxal and 3-hyroxypropanal.

ACPD
11, 9887–9957, 2011

1 Introduction

Formaldehyde (CH_2O) is an important and ubiquitous trace gas found throughout the atmosphere. This gas, which is the most abundant carbonyl compound found in the atmosphere, is formed from the oxidation of most anthropogenic and biogenic hydrocarbons, primarily initiated by reactions with the hydroxyl (OH) radical and ozone (O_3). Formaldehyde is also directly emitted into the atmosphere from biomass burning (Lee et al., 1997); incomplete combustion from motor vehicles (Herndon et al., 2005), potentially from petrochemical flares (Olaguer et al., 2009) and other sources; industrial emissions, and by emissions from vegetation (Carlier et al., 1986, and references therein). Typical atmospheric mixing ratios vary from approximately 1 part-per-billion by volume (1 ppbv, 1 part in 10^9 parts of air) in the background continental boundary layer (Harder et al., 1997) to several 10's of ppbv for polluted air over urban regions (Dasgupta et al., 2005) and air influenced by petrochemical refinery emissions (primarily ethene and propene) during summer months (Wert et al., 2003). In the remote background atmosphere by contrast, the oxidation of methane (CH_4) becomes the dominant source of CH_2O. In these cases, ambient CH_2O mixing ratios are typically on the order of several hundred parts-per-trillion by volume (1 pptv, 1 part in 10^{12} parts of air) near the surface, and on the order of 50 pptv or less in the upper troposphere above 8 km (Fried et al., 2003b). Formaldehyde is also produced from numerous other precursors including methyl hydroperoxide (CH_3OOH, MHP), methanol (CH_3OH), and isoprene, to name a few compounds.

Formaldehyde primarily decomposes via three pathways, two involving photolysis and one with OH. At wavelengths less than 339-nm the quantum yield for the radical photolysis channel ($2HO_2 + CO$) is non-zero and this channel becomes dominant at wavelengths less than about 324-nm, while at longer wavelengths than this but shorter than 361-nm the molecular decomposition channel ($H_2 + CO$) becomes dominant (Sander et al., 2006). Under certain circumstances (high altitudes, large solar zenith angels and/or dry conditions), the radical photolysis channel of CH_2O can dom-

ACPD
11, 9887–9957, 2011

inate over other radical production pathways. In the presence of sufficient NO, the added HO_2 radicals from this channel results in the production of ozone. In Mexico City, CH_2O photolysis is responsible for about 20–25% of radicals on a 12-h average daytime basis (Dusanter et al., 2009; Volkamer et al., 2010), and hence adds substantially to the efficient formation of ozone and secondary organic aerosols (SOA) (Lei et al., 2008). Lei et al. (2009) further report that primary CH_2O in the Mexico City Metropolitan Area enhances daytime radical production and peak ozone concentrations by up to 10% and 8%, respectively.

Because of the relatively short lifetime of CH_2O (several h at mid-day), it is a good tracer for recent photochemical activity of hydrocarbons. Since CH_2O is produced as an intermediate from the oxidation of many hydrocarbons, this gas also serves as an important test species in evaluating our mechanistic understanding of tropospheric oxidation reactions, which is often done through comparisons of time coincident CH_2O observations with box models. Numerous studies have been devoted to this topic, and recent examples include Fried et al. (2003a, b), Fried et al. (2008a, b), Kormann et al. (2003) and references therein, and Junkermann et al. (2009). As discussed in these references, box models have at times: underestimated, overestimated, and accurately simulated CH_2O observations, depending upon the measurement regime.

In the lower troposphere typically below 2 km, box models have often underestimated CH_2O observations. This problem is particularly acute in the presence of fresh emissions (Fried et al., 2003b, 2008a), either fresh emissions of CH_2O and/or its short-lived precursors such as ethene and isoprene. The modeling studies listed above have used a steady-state modeling approach that is constrained by in-situ measurements of precursor species. This approach does not include direct CH_2O emission sources and is limited to instantaneous measurements of non-methane hydrocarbons and other precursors, so in the vicinity of large and relatively fresh emissions, this approach may underestimate the recent history of photochemical production of CH_2O from very short-lived hydrocarbons during rapid decay just prior to the point of measurement. In the case of isoprene, furthermore, CH_2O will continue to be produced

ACPD
11, 9887–9957, 2011

from higher generation isoprene oxidation products even when the parent isoprene molecule has decayed away, resulting in model underestimations many h after emission. The steady state modeling approach is also dependent upon the availability of measurements of important CH_2O precursors such as MHP and methanol. In the case of fresh pollution, unmeasured hydrocarbon species may present another model limitation. In addition, it becomes more important to assure precise data overlap within fresh plumes. Timescales for data averaging that are typically used for modeling purposes (e.g., 1-min) may not be sufficient to capture ambient high-resolution data variability. In fact, the four largest CH_2O measurement/model ratios observed during the INTEX-NA study (Fried et al., 2008a) all resulted from poor temporal overlap between CH_2O and its precursors. Fried et al. (2003b) have also shown that when physical sink processes are missing from models, such as the uptake of CH_2O and MHP within clouds and in the lower marine troposphere, box models can overestimate observations. However, in the absence of these effects, Fried et al. (2003b, 2008a) have also shown that despite point-to-point scatter, on average one can obtain good overall agreement between CH_2O measurements and box model calculations away from local sources in the mid to upper troposphere. Because of the short CH_2O lifetime local emission sources become less important in these regimes. This implies that several CH_2O lifetimes away from such sources and sinks we generally have a good understanding of CH_2O chemistry in the background mid to upper troposphere.

However, the various studies by our group, employing observations based on tunable diode laser absorption spectroscopy, and by other groups continue to point to persistent unresolved model underestimates of CH_2O in the boundary layer (operationally defined here as radar altitudes between the surface and 2 km), and this includes air masses far from local emission sources. During INTEX-NA (Fried et al., 2008a), for example, model underestimations by approximately a factor of two were observed in the boundary layer over the Atlantic Ocean over 1000 km from the nearest land source. Such discrepancies during the TRACE-P (Fried et al., 2003b) and INTEX-NA (Fried et al., 2008a) studies progressively increased with increasing ambient CH_2O levels. Over

ACPD
11, 9887–9957, 2011

the Gulf of Mexico and the remote tropical Pacific Ocean, unexplained and high concentrations of CH_2O and other oxygenated VOCs have been observed in the boundary layer up to 3000 km from land (Sinreich et al., 2010; Coburn et al., 2011). Over the continental United States during the INTEX-NA study, median box model results underestimated median CH_2O observations by as much as ~700 pptv in the boundary layer (Fried et al., 2008a). In addition to the possibility of systematic measurement errors from spectroscopic interferences and errors caused by poor temporal overlap between CH_2O observations and model inputs, which are primarily dependent upon the hydrocarbon (HC) precursors, the boundary layer discrepancies could also arise from: unmeasured hydrocarbons; non-steady state environmental conditions, such as may occur near large pollution sources; direct CH_2O emissions and transport of such direct emissions; processes which are not included in the box model such as production from heterogeneous/multiphase oxidation or losses to aqueous phases; and CH_2O production from the breakdown of reactive intermediates that are formed via multi-generation oxidation processes, analogous to the formation of SOA; or some combination of these.

The present airborne study over Mexico (including Mexico City), the Gulf of Mexico, parts of the continental United States near the Gulf coast, as well as the more remote Pacific Ocean, provides an additional opportunity to further examine CH_2O measurement-box model relationships over a wide geographic range spanning measurements near the surface to 12 km and over widely differing CH_2O regimes.

2 Overview of present study

Data for the present study was acquired onboard the NASA DC-8 aircraft during the Intercontinental Transport Experiment-Phase B (INTEX-B) study, as part of the 2006 MILAGRO campaign, which took place in the spring (4 March–15 May) of 2006 (Singh et al., 2009; Molina et al., 2010). This paper primarily focuses on comparisons in the boundary layer, with an emphasis on comparisons very close to large emission sources and comparisons during air mass aging in Mexico City outflow events. In particular,

ACPD
11, 9887–9957, 2011

the present study examines CH_2O measurement-model discrepancies as a function of photochemical processing times. Formaldehyde comparisons above the boundary layer and over more remote regions of the Pacific Ocean will also be discussed to provide contrasting behavior.

There were two independent CH_2O instruments operating on the DC-8: a tunable diode laser absorption spectrometer (TDLAS) developed and operated by our group at NCAR (see Appendix A) and an enzyme fluorescence detection (EFD) system developed and operated by the University of Rhode Island. A discussion of past comparisons between these two instruments can be found in Fried et al. (2008a) and references therein. Although comparisons between these two instruments are indeed important, this will be the topic of other papers (Kleb et al., 2011 as one example). The present study exclusively focuses on CH_2O measurements acquired by the TDLAS system. The long continuous history of such measurements with box model comparisons using the same measurement methodology spanning nine years allows us to assess measurement-model relationships in a more straightforward way as functions of geographic region and time. In addition, for reasons that will become clear, fast 1-s airborne CH_2O measurements possible with the TDLAS system are an important aspect of the present study where temporal overlap between measurements and box model inputs are considered.

The INTEX-B study was carried out in two phases: the first phase (4 March–22 March), which is shown by blue flight tracks in Fig. 1, focuses on Mexico, the Gulf of Mexico, and the Gulf coast of the United States. The second phase (17 April–15 May), which is depicted by the red flight tracks, focuses on the remote Pacific Ocean and coastal regions of Alaska. Although this study employs the same CH_2O TDLAS measurement approach as TRACE-P and INTEX-NA studies and the same box modeling approach, a number of improvements have been incorporated into the present comparisons, and this can provide additional information about the sources of these boundary layer discrepancies. First, a number of enhancements to the TDLAS system were implemented, resulting in improvements to measured CH_2O detec-

ACPD
11, 9887–9957, 2011

tion limits by an average factor of 1.6 relative to the INTEX-NA study. It is important to note that these improvements only affect measurement precision and not overall measured CH_2O mixing ratios. Secondly, to eliminate the issue of poor temporal overlap between CH_2O measurements and the model inputs, which are primarily dependent upon the hydrocarbon (HC) precursors, we consider here comparisons on the HC time base rather than comparisons based solely on the official 1-min merged data (http://www-air.larc.nasa.gov/missions/intex-b/intexb.html). To accomplish this, 1-s CH_2O TDLAS measurements were integrated over the start and stop times of the HC database. We also derive a more restricted dataset where the measurements comprised at least 50% of the HC time base and where the measurements were uniformly distributed over this time base. This restricted dataset was further limited to time periods where there were MHP measurements to constrain the box model (see Fried et al., 2003b and 2008a and references therein for the importance of this).

To address the potential issue of systematic measurement errors due to unknown spectroscopic interferences, we will show comparisons of boundary layer CH_2O measurements acquired by the TDLAS system during DC-8 overflights over Mexico City ground-based supersites where there were independent CH_2O measurements based upon in situ Hantzsch liquid phase fluorometric detection systems as well as MAX-DOAS systems. Additional comparisons between airborne spectroscopic CH_2O measurements and these two ground-based systems were also carried out using a newly developed difference frequency generation (DFG) instrument developed by our group operating on the NCAR C-130 aircraft. Even though this DFG system was based on a different laser source than the DC-8 TDLAS system, both instruments use the same CH_2O absorption feature, have similar laser linewidths, employ the same calibration, measurement, zeroing, and fitting approaches, and thus any systematic error in one in all likelihood should also be reflected in the other. The airborne intercomparison of these two instruments (not blind in this case) on 19 March when the DC-8 and C-130 were flying in close formation near Mexico City produced a linear regression (TDLAS versus DFG) slope of 1.018 and an intercept of 3 pptv (measurement range ~500 pptv

ACPD
11, 9887–9957, 2011

to 3500 pptv). The 1 s TDLAS measurements were averaged over the 30-s DFG time base for this comparison. The comparisons of this study also include a careful re-assessment of model uncertainties. In previous comparisons during INTEX-NA and TRACE-P (Fried et al., 2008a and 2003b), we adopted the model sensitivity analysis of Frost et al. (2002) to arrive at an approximate model random uncertainty of 24% (2σ) times the model mixing ratio. The general approach of Frost et al. (2002) is used here to estimate the component of model uncertainty due to uncertainties in input constraints, utilizing environmental conditions and instrument uncertainties appropriate for the INTEX-B campaign. A Monte Carlo approach, using selected environmental and chemical conditions typical of geographical regions encountered during INTEX-B, is used to estimate the component of model uncertainty due to kinetic and photolytic rate uncertainties. More comprehensive discussions of the TDLAS measurement, steady state box model, and the measurement and modeling uncertainties can be found in Appendix A.

3 Comparisons of airborne CH_2O measurements with ground-based measurements

We have a long history of measurement comparisons between the present TDLAS system and earlier versions of this system with other CH_2O measurement approaches, and discussions for which can be found in Appendix B. During the present study there were a total of nine different time periods when either the DC-8 or the C-130 passed close to ground sampling sites over Mexico City and where there was evidence of sampling in the same air mass as ground-based CH_2O measurements acquired by either Hantzsch or DOAS systems. Appendix C and tables therein further discuss such comparisons, and the results are summarized in Fig. 2. The airborne DC-8 and C-130 CH_2O spectroscopic measurements are plotted on the Y-axis as a function of the two ground-based measurements, and different comparisons are displayed using different symbols. As can be seen, the agreement among the measured/derived CH_2O values is excellent: all 4 CH_2O mixing ratios fall on line with a slope of 0.97 and near zero intercept. This is

ACPD
11, 9887–9957, 2011

consistent with the agreement obtained in past TDLAS-Hantzsch comparisons (Gilpin et al., 1997), past TDLAS-DOAS comparisons (Harder et al., 1997; Wert et al., 2003), and past Hantzsch-DOAS comparisons (Hak et al., 2005), and provides additional confidence in the present airborne TDLAS measurements.

4 Measurement-steady state box model comparisons

Figure 3 shows a plot of the cumulative percentage measurement/model ratios and (measurement-model) differences for the three different merge time bases discussed in the Introduction for the NASA DC-8 employing the TDLAS measurements. In the measurement-model comparisons of this study we will show both the ratios and differences since each one has a drawback that can mask the true level of agreement: the ratio becomes unduly sensitive at low model values and the differences can be unduly large at high mixing ratios, which may in part reflect laser wavelength instabilities and/or the presence of spectral interferences. Figure 3 shows that large differences between the different merge time bases are only observed in the ratios and differences for the lowest and highest 5% of the comparisons, indicating that the timescale for averaging is not that important, at least in the present study, for most of the comparisons. Unless indicated otherwise, this study employs DC-8 comparisons on the hydrocarbon time base; the more restricted data set reduces the number of boundary layer comparisons in the first phase from 347 down to 136 data points. Figure 3 shows that the median measurement-model ratios and differences in the boundary layer range between 1.32 to 1.34 and 332 to 352 pptv, respectively, for the 1st mission phase for the three different data sets. A similar figure for C-130 comparisons using only the 1-min merged data set (not shown), reveals similar but slightly higher discrepancies (median ratio of 1.47 and a median difference of 544 pptv). The median boundary layer measured values for the DC-8 and C-130 are, respectively 1532 pptv and 2262 pptv, and the higher C-130 value no doubt plays a role in the higher C-130 discrepancies.

Figure 4 plots radar altitude binned median DC-8 measurement and box model time-coincident results for both phases of INTEX-B on the hydrocarbon time base along with

ACPD
11, 9887–9957, 2011

the number of comparisons. Eight radar altitude bins are used: 0–0.5 km, 0.5–1 km, 1–2 km, 2–4 km, 4–6 km, 6–8 km, 8–10 km, and 10–12 km. Table 1 further tabulates the TDLAS-box model comparisons, which also includes differences and ratios determined from the point-to-point comparisons. As can be seen large model underestimates are again observed for the three altitude bins below 2 km during the first mission phase, which focuses on Mexico, the Gulf of Mexico and the Gulf coast of the United States. The point-to-point comparisons of Table 1 also reveal model CH_2O underestimation in the 2 to 4 km altitude range, which is not apparent in the plot of the medians. By contrast during the second phase, which was primarily over remote regions of the Pacific Ocean, the median TDLAS measured and modeled CH_2O mixing ratios as well as point-to-point differences are all in good agreement at all altitudes, as further shown in Table 2. This is in contrast to boundary layer comparisons over the open Atlantic Ocean during INTEX-NA. In the 0 to 0.5 km bin, Fried et al. (2008a) report a median measurement/model ratio of 1.56 compared to a ratio of 1.15 observed in this study over the generally cleaner Pacific Ocean. As mentioned previously, we believe this difference reflects the effects of North American outflow of CH_2O precursors, which as will be shown later, can last several days downwind from the emission source. Although Pacific measurement-model ratios in this study are near 0.5 for the 3 altitude bins between 4 and 10 km, the differences are small ranging between −35 and −27 pptv.

The comparisons of Fig. 4 raise the following question: are the observed TDLAS-box model boundary layer discrepancies during the first phase outside the combined measurement-model uncertainty estimates? This is addressed in Figs. 5–8 where we plot altitude binned time coincident TDLAS measurement-model comparisons for four different geographic locations spanning both mission phases. We display the median TDLAS measurement and box model mixing ratios for each altitude bin (left side) along with the number of comparisons points, the median and individual point-to-point measurement/model ratios (center), the median and individual point-to-point (measurement-model) differences (right side). Also shown on the figures is the range of combined random measurement uncertainty and model constraint uncertainty

ACPD
11, 9887–9957, 2011

expected for a given altitude bin at the 2σ level. Figures 5–7 primarily reflect comparisons during the 1st phase while Fig. 8 exclusively reflects comparisons during the 2nd phase. It is important to note that a given combined uncertainty in the difference represents an increasingly larger uncertainty in the ratio with altitude because of the decreasing absolute CH_2O concentration values.

To account for the possibility that the TDLAS instrumental precision may be somewhat poorer in the boundary layer due to elevated CH_2O levels, turbulence, and larger swings in cabin environmental conditions of temperature and pressure, which could potentially produce greater laser wavelength instabilities, we consider here the possibility that measurement imprecision limits in the boundary layer discussed in Appendix A may be higher than LOD estimates. To estimate the potential magnitude of this, we compare measurement precisions from the normalized 1-s data in the boundary layer with the in-flight-determined LODs based on all altitudes. For mixing ratios in the 1–2 ppbv range, this produced boundary layer measurement precisions a factor of 1.4 to 2 times the in-flight-determined LOD values. Although this procedure also folds in more ambient variability than the LOD determinations, it provides the most conservative upper limit to the instrument precision in the boundary layer. These modified precision estimates were folded into the combined uncertainty estimates shown in Figs. 5–8. Likewise the model constraint uncertainty limits for the various altitude bins represent conservative upper limits here since we have not folded in the possibility that altitude bin-averaging of multiple data points may improve the overall model uncertainty, as suggested by independent Monte Carlo calculations. This would also apply to the CH_2O measurements. Nevertheless, the combined uncertainty bounds of Figs. 5–8 yield conservative upper limits beyond which CH_2O measurement and model constraint uncertainties cannot explain the discrepancies.

In Fig. 5, which depicts comparisons over the continental United States and Mexico (exclusive of Mexico City and Monterrey), one observes model underestimates in both the ratios and differences below 3 km. The discrepancy peaks in the 0.5–1 km bin but is not evident in the 0–0.5 km bin. For altitude bins greater than 3 km, the ratios

ACPD
11, 9887–9957, 2011

and differences fall within the mutual uncertainty limits. As the combined uncertainty estimates previously discussed are conservative upper limits, the 0 to 3 km discrepancies clearly fall outside the combined uncertainty range for any realistic uncertainty scenario. Although these discrepancies do fall within the combined systematic error estimates (not shown), which include instrumental systematic error estimates and *model kinetic uncertainty* estimates (see Appendix A), the boundary layer comparisons of Fig. 5 reveal a problem that cannot be explained by systematic uncertainty bounds. Considering the lowest two altitude bins for example, one cannot use systematic errors to explain near agreement in one altitude bin and large disagreements in an adjacent altitude bin where the bin-averaged temperatures and pressures only change by 1.7% and 7.4%, respectively.

The Mexico City and Monterrey plots of Fig. 6 likewise show model underestimations between 0.5 to 2 km, and agreement in the lowest altitude bin. As will be further discussed, samples in this bin are from very fresh plumes, and as such, steady-state modeling may not be appropriate. At altitudes from 3 km and greater all 3 plots of Fig. 6 show measurement-model agreement within or just lying on the combined uncertainty bounds with the exception of the ratio in the 6 to 8 km bin. This is an artifact of the small number of points ($N = 2$) here. The Gulf of Mexico data of Fig. 7 shows model underestimates for all three low-altitude bins up to 2 km. As will be discussed later, only about 12% of these points originate from Mexico City outflow. In the 2–4 km bin, the median ratio and median difference values are very close to the mutual uncertainty bound yet the median measurement and model values on the left indicate perfect agreement. This is a case where the point-to-point comparisons reveals a potential problem in our understanding but is hidden by the simple comparison of medians, and this emphasizes the importance of employing all three comparison plots when assessing measurement-model agreement. Like the previous figures, at higher altitudes than 4 km the measurements and model values are in agreement for all three plots.

ACPD
11, 9887–9957, 2011

The Pacific Ocean plots of Fig. 8 show excellent measurement-model agreement in the medians over all altitude bins, despite individual comparisons falling outside the estimated mutual uncertainty limits. This figure provides further evidence supporting the conclusions of past studies: namely, that in the remote background atmosphere away from local sources and sinks we generally have a good understanding of CH_2O chemistry, despite larger measurement variance than modeled. By contrast, the systematic discrepancies observed in the boundary layer over the continental United States, Mexico and the Gulf of Mexico, again suggests that as in past studies, one or many of the aforementioned issues presented in the Introduction may be operative. As previously discussed, we do not believe that systematic uncertainties in gas phase reaction rate constants are the cause for such discrepancies.

Figure 9 further examines the boundary layer discrepancies during the 1st phase as a function of map location. Here the measurements on the hydrocarbon time base are colored and sized by the measured mixing ratios. To preserve resolution this scale only extends up to 6000 pptv. However, there are plumes over the Gulf of Mexico and over Mexico City that extend up to 14.6 ppbv. It should be noted that these measurements are averaged on the hydrocarbon time base, which is typically on the order of 1 min or more. Peak plume durations, however, are only s to 10's of s long and thus true ambient CH_2O mixing ratios can be significantly higher than those in Fig. 9. For example, our 1-s measurements indicate that the 14.6 ppbv Mexico City plume attains values as high as 28.6 ppbv. We also plot in Fig. 9 the various point VOC emission sources (sized by their VOC emission rates in tons yr^{-1}) as well as average measurement/model ratios and standard deviations for various geographic flight segments (data close in time and geographic location) highlighted in circles. It is useful to keep in mind that the upper quartile value for the combined estimated measurement-model ratio uncertainty in the boundary layer is 1.18, and thus many of the averaged ratios over these domains are systematically high.

Over Mexico City and Monterrey the averaged flight segment measurement/model ratios in the boundary layer are 1.2 while the ratios over the Gulf are primarily in the

ACPD
11, 9887–9957, 2011

1.2 to 1.4 range; indicating small to modest model underestimates on average over these regions. Near the largest VOC emission sources northeast of Mexico City and over Western Alabama (several h downwind of a large power plant), the flight segment ratios are in the 1.6 to 1.9 range; indicating larger model underestimates. By contrast, over parts of Texas and the Pacific Ocean side of Mexico the ratios are closer to unity. Although Fig. 9 provides a general sense where larger measurement-model discrepancies are observed, it does not provide further information regarding the cause of such discrepancies other than the fact that the largest discrepancies do not in general correlate with the highest CH_2O mixing ratios. In fact, the measurement-model ratios of Fig. 10 show more clearly that better agreement tends to be obtained at higher ambient CH_2O mixing ratios. This plot displays the median and averaged ratios binned by model values for both the boundary layer (colored filled points) and outside the boundary layer (open black circles). In the boundary layer the medians are colored and sized by the median alkene production percentage from the model, and the numbers next to each point represent the number of points in the bin (top number) and the binned median photochemical age (bottom number). The photochemical age was determined from the ratio of 2-butyl nitrate to butane, as discussed by Bertman et al. (1995) and Perring et al. (2010). This age determination will hereafter be referred to as butane times or photochemical age. In these calculations we employ the instantaneous measured DC-8 OH mixing ratios using the laser induced fluorescence technique (Ren et al., 2008; Mao et al., 2009). Although there is more uncertainty in the precise photochemical age for more aged air using instantaneous OH values, this procedure still yields correct relative ages. The gray shaded region represents the median for the combined measurement (random uncertainty) and *model constraint uncertainty* at the 2σ limits in the CH_2O ratio for the boundary layer (±13%). Binned values inside this band fall within the expected uncertainty limits.

As Fig. 10 shows, the median boundary layer ratios in the lowest four model mixing ratio bins (0 to 2000 pptv) yield high median measured-to-modeled ratios extending from 1.28 to 1.46, and these fall outside the described uncertainty limits. Although not

ACPD
11, 9887–9957, 2011

shown, the first four model bins yield median (measurement-model) differences in the point-to-point comparisons from 164 pptv to 517 pptv. The alkene production percentage extends from 4 to 20% for these points while the binned median photochemical age ranges between 42 and 14 h. The 3 highest binned non-boundary layer points (500–2000 pptv) show discrepancies comparable to those in boundary layer and this is to be expected since the binned median altitudes for these points, which are primarily over the Gulf of Mexico and Mexico, (radar altitudes of 2.4 to 2.8 km) are all close to our 2 km boundary layer cutoff and ~60% of these comparisons are from outflow events from the Mexico City boundary layer (to be discussed); Figs. 5–7 further show that measurement-model discrepancies over these two regions are actually observed over a range of altitudes below and slightly above our 2 km boundary layer cutoff. By contrast, the 5 lowest non-boundary layer binned points spanning the 0 to 500 pptv range yield measurement-model agreement to within 13% (median radar altitudes are all above 3 km) and only 7% of these comparisons are from Mexico City boundary layer outflow events. The 3rd non-boundary layer point spanning the 200 to 300 pptv range yields agreement (median bin ratio = 1.06, $N = 32$, median radar altitude = 3.3 km) while its boundary layer counterpart spanning the 0 to 500 pptv shows a large measurement-model discrepancy (median bin ratio = 1.46, $N = 25$, median radar altitude = 1.3 km). It is thus apparent that the higher altitude binned data out of the boundary layer reflects entirely different behavior than within the boundary layer, indicating that the measurement of CH_2O mixing ratio is not the primary factor affecting the agreement. It is interesting to note that the BL discrepancies observed here with ambient CH_2O mixing ratios starting at values around 250 to 500 pptv are consistent with our TRACE-P (Fried et al., 2003b) and INTEX-NA (Fried et al., 2008a) results; in these cases discrepancies were observed when binned model values exceeded mixing ratios of ~350 pptv.

However, as Fig. 10 suggests there are additional factors at play when ambient CH_2O mixing ratios exceed ~2 ppbv; here median binned alkene CH_2O production percentages increase to values greater than 28% and median processing times decrease

ACPD
11, 9887–9957, 2011

below 6 h. Although methane dominates CH_2O production in the boundary layer for the 4 lowest mixing ratio bins, production from alkenes and RCO_3-type compounds (PAN and higher acetyl peroxy compounds) becomes dominant in the model for the six highest mixing ratio bins. The alkenes, which are comprised of ethene, propene, isoprene, 1-butene, trans-2-butene, cis-2-butene, and 1,3-butadiene, is dominated in all cases by CH_2O production from ethene. Starting at the 5th boundary layer bin (model midpoint = 2250 pptv) and extending to the highest mixing ratio bin, over 80% of the alkene production of CH_2O originates from ethene. This is consistent with the ground-based measurements reported by Apel et al. (2010) at the T_0 site where ethene was found to comprise 65% of the total alkenes listed above on a 24-h bias throughout the month of March. As can be seen in Fig. 10, the six highest model bins result in measurement/model ratios near or within the uncertainty band, and under these conditions the observations included as model inputs appear to accurately represent the dominant ambient chemistry. However, a closer look shows that for the highest bin, the model slightly overpredicts the observations by up to 18%, and this suggests that very close to large sources of NMHCs (primarily ethene), the model's diurnal steady state assumption is inadequate, resulting in significant overpredictions of CH_2O generated from ethene. While it is not expected that the steady state model should be able to accurately calculate CH_2O under non-steady-state conditions, it is instructive to examine the non-steady-state influences in closer detail. Further downwind of pollution sources, where the fast-reacting ethene has largely decayed away, the model underpredicts the observed CH_2O. Thus, in the vicinity of high ethene sources, non-steady state conditions can result in different measurement-model behavior depending upon the processing time, and this will be further discussed in the next section. At low mixing ratios, by contrast, the measurement/model ratios of Fig. 10 suggest the influence of the other effects raised in the Introduction. These effects are apparently masked when fast CH_2O production from ethene and RCO_3-type compounds (PAN and higher acetyl peroxyl compounds) becomes more dominant in the vicinity of fresh plumes.

ACPD
11, 9887–9957, 2011

Considering only points with low contributions to total CH_2O production from ethene (production <12%), the average and median measurement/model ratio of ~1.2 previously discussed in connection with Fig. 9 in the Mexico City boundary layer reduces to 0.96. Although this restricted comparison is based on only 10 points on the hydrocarbon time base, it indicates that the model accurately reproduces the observations in the boundary layer over Mexico City and that unmeasured hydrocarbons and direct CH_2O emissions from vehicle traffic have minimal effect on the predicted CH_2O in this case. In the case of the latter this can only come about if the observed CH_2O over the city is primarily from oxidation of CH_2O precursors, as the model does not include direct CH_2O emission sources. This is consistent with the fact that local sampling times for DC-8 overflights in the Mexico City boundary layer took place outside of rush hour time periods (11:29–14:20 on Monday–Saturday), when source apportionment studies find ~80 to 99% of ambient CH_2O is from secondary sources (Garcia et al., 2006; Volkamer et al., 2010). The importance of secondary CH_2O is further corroborated from our fast (1-s) CH_2O correlations with CO_2, which produce regression slopes with factors of 3–4 times higher than those measured by Herndon et al. (2005) during ground-based vehicular traffic ("vehicle chase") studies in Mexico City. We can further use the median photochemical age as well as the median CH_2O lifetime to eliminate the possibility that direct CH_2O emissions are responsible for most of the measurement-model disparities in the four lowest boundary layer bins of Fig. 10. In these bins, 91% of the comparisons were either over the Gulf of Mexico (54%) or over continental Mexico and/or the United States (37%) outside of major urban centers. The median photochemical age was at least 14.8 h for these points, which when compared to a median CH_2O lifetime of 2.4 h indicates that any direct CH_2O emissions would have decayed to values well below the observed discrepancies. We will return to the boundary layer discrepancies of Fig. 10 for mixing ratios <2 ppbv after we discuss the temporal behavior of fresh boundary layer plumes with much higher mixing ratios.

At typical DC-8 overpass times over the City the photolysis of secondary VOC oxidation products including CH_2O is responsible for ~52% of overall radical production

ACPD
11, 9887–9957, 2011

(Volkamer et al., 2010), and for an even higher percentage on a daytime average basis (Dusanter et al., 2009; Volkamer et al., 2010). Primary emissions of CH_2O (Herndon et al., 2005; Garcia et al., 2006) are most relevant to sustain photochemical activity in the mid-morning (Lei et al., 2009; Volkamer et al., 2010), but become dominated by secondary CH_2O sources already over ageing time scales of a few hours (Garcia et al., 2006; Volkamer et al., 2010). This emphasizes the relevance of secondary sources of pollution to sustain the production of ozone and SOA already in the chemical near field over Mexico City.

5 Temporal behavior of CH_2O in fresh boundary layer plumes

The temporal behavior of CH_2O observations in fresh boundary layer plumes in the presence of high ethene mixing ratios and where precursor values are rapidly changing cannot be adequately reproduced using diurnal steady state (DSS) modeling assumptions. However, an examination of the inadequacies of such a modeling approach can highlight dominant processes leading to CH_2O production in such environments. As will be shown, the DSS box model systematically overestimates observations of CH_2O in plumes very close to emission sources high in ethene. The DSS assumption constrains values of ethene to the instantaneous observed value throughout the model day, resulting in model overestimates of CH_2O. At sustained very high ethene concentrations, the model will significantly overestimate concentrations of product species with moderate lifetimes, such as acetaldehyde and higher aldehydes. In essence, it takes a finite amount of time for the model to properly *spin-up.* As the plume age approaches the ethene lifetime (around 3–7 h over Mexico City), the model starts to underestimate the observations of CH_2O. This latter effect is a result of another permutation of non-steady-state conditions: namely, it reflects the fact that the instantaneous measurement of ethene used in the box model does not account for the temporal history of CH_2O recently produced by the rapidly decaying ethene. For intermediate processing times close to the CH_2O lifetime one would expect the measurement-model to cross the value of 1.

ACPD
11, 9887–9957, 2011

Figure 11a displays one such example of the temporal dependence of the CH_2O measurement/model relationship due to ethene for various plume ages. This figure shows a time series plot of the CH_2O measurements and model results along with corresponding 2σ uncertainty limits. These data were acquired over the center of Mexico City on 16 March 2006 where back trajectory analysis indicated that the sampled air at the peak mixing ratio was approximately 2 h downwind of two of the largest VOC emission sources in the center of the city (a facility that manufactures industrial food packaging and one that makes polyester additives). Some of the points in Fig. 11a comprise points in the highest bins of Fig. 10. We designate above each point in Fig. 11a the measurement/model ratio and the photochemical age. It is important to note that the 2.2 h age from this analysis is in agreement with back trajectory analysis (see Martin et al., 2003 for a discussion of this approach). The CH_2O observations in Fig. 11a are also colored and sized by the ethene production percentage from the box model. The behavior in this figure, with a few exceptions, is in line with the expectations discussed above. Figure 11b better displays this behavior for these same points by plotting the measurement/model ratio as a function of photochemical age. The 15 points most influenced by CH_2O production from ethene (photochemical age $\leq$6.1 h and ethene production percentage $\geq$12%, $N = 15$) are emphasized by their color and size and are fit using a 3-term polynomial shown in blue (Profile 1). A linear fit, which would be equally valid, yields essentially the same behavior with some small differences. Boundary layer flight legs over central Mexico City on other days are very similar with only slightly different shapes and intercepts, dictated by the ethene and CH_2O lifetimes.

The red curves in this figure represent results from an exercise that tests the box model steady state assumption against output from a Lagrangian model that simulates non-steady state chemistry in a plume with rapidly decaying ethene. The Lagrangian model was initialized using values observed on the DC8, and then a "pulse" of NMHCs was introduced to simulate an emission source. The chemistry was allowed to evolve in a Lagrangian, time-dependent fashion with all model constraints relaxed.

ACPD
11, 9887–9957, 2011

The calculations assumed a concurrent "pulse" of NO_x and various NO_x mixing ratios from 0 to 25 ppbv were assumed. The "pulse" value of NMHCs was set equal to their observed values at the peak of Fig. 11a [ethene (8.8 ppbv), isoprene (53 pptv), and other alkenes (1360 pptv)] on 16 March 2006 and were introduced into the model in the morning at sunrise. Output from the Lagrangian model was then taken at various times, and fed into the steady-state box model to test the fidelity of the steady-state approach under various plume processing times. The ratio of the Lagrangian to steady state box model CH_2O is plotted as a function of these processing times on the same axis as the measurement-model comparisons. The Lagrangian-to-steady state ratios serve as a proxy for the measurement/model ratios in indicating the influence of non-steady-state conditions. The spread in these results, given by the red bounds for the two curves, represent the maximum and minimum in these calculations for the various NO_x scenarios. This plot simulates the behavior of the box model in calculating CH_2O when sampling a large time dependent ethene plume in the near-field, in this case from factory sources. Only slightly different behavior is observed when the ethene spike is introduced at different times of the day. We designate the bounded red curves as Profile 2.

Although there are clear differences between the two profiles, there are also some important similarities. At zero processing time, the simulations of Profile 2 span the Y-intercept value of Profile 1 (0.26 ± 0.47), and the photochemical age where 1:1 measurement/model agreement is obtained in Profile 1 (~2.0 h) is spanned by the range of values from Profile 2. In fact, we observe the expected measured/model CH_2O behavior as a result of non-steady-state conditions out to ~4 h of processing with ratios approaching 1.6. Thus, in fresh ethene dominated plumes one must recognize such time-dependent behavior where one can obtain steady-state model overestimations, underestimations, and agreement with the observations depending upon the processing time. Although the curvature will be different for different alkene plumes, one should expect very similar behavior to Fig. 11b. This behavior explains the measurement/model ratios for the largest 6 bins of Fig. 10 as a result of non-steady state

ACPD
11, 9887–9957, 2011

conditions. At processing times longer than ~4 h, the two profiles of Fig. 11b show differences; here the observations to box model ratios continue to rise compared to the Lagrangian time dependent simulations, which level off and start to decay as the influence of fast reacting alkenes abate. These differences most likely reflect the additional influence of dilution, additional hydrocarbon sources of CH_2O, which become more important as the plume ages, and the imperfect atmospheric simulation here using the simple Lagrangian model. Although not as obvious as the 15 points in Fig. 11b, the effects of ethene are still seen in the Lagrangian/box model simulations out to processing times as long as ~12 h for these ethene simulations (ethene lifetime here = 6.8 h). At much longer processing times and/or low ethene production contributions, as shown by the inset and the additional 5 points of Fig. 11b, the effects of ethene are no longer evident for this 16 March plume.

6 Mexico City outflow and evidence for unmeasured hydrocarbons and multi-generation CH_2O oxidation processes

Thus, although we can explain the CH_2O TDLAS measurement-model relationships as an artifact of the steady state assumption for short transport times where ethene production dominates, this cannot explain the boundary layer behavior of Figs. 9–11 whenever the transport times exceed ~8 h and where other sources of CH_2O other than ethene may dominate. Many of the Gulf boundary layer legs of Fig. 9 are examples of this and Fig. 10 further hints at the importance of photochemical age. In this section we focus our discussion on Mexico City outflow events in order to further examine CH_2O measurement-model relationships as a function of plume age. In addition to showing the influence of Mexico City on CH_2O budgets and hence on radical budgets downwind, this analysis also attempts to elucidate the production mechanisms of CH_2O in an aging plume when the non steady-state influences of local sources are minimized. Although we can carry out this same analysis for all boundary layer plumes, including the myriad of plumes originating from Gulf oil platforms and production facilities, restricting this

ACPD
11, 9887–9957, 2011

to Mexico City boundary layer outflow plumes has two main advantages: (1) the input hydrocarbons are better characterized since we have available the Mexico City network of fully instrumented sampling sites (T_0, T_1, and T_2) as further discussed by Apel et al. (2010), and (2) the characteristics of these outflow plumes can be further explored to ensure that fresh local pollution sources do not have large impacts on the plume composition as the plume ages. Although individual outflow comparison points can indeed be affected by such local sources, the binning procedure on average reduces such influence.

Mexico City plumes were identified using the same approach as Perring et al. (2010). In this case we employed the official 1-min merged data set instead of the merge on the hydrocarbon time base. As discussed by Perring et al. (2010), back trajectories were used to select data that passed within ~ 100 miles (1.5°) of the T_0 sampling site in the center of Mexico City at pressures higher than 680 mb, which corresponds to an elevation of ~1 km above the ground over Mexico City (Mexico City elevation is 2240 m and the typical surface pressure is ~770 mb). Of the 422 time periods identified by Perring, 262 time periods had simultaneous CH_2O TDLAS measurements and model results where there were also calculations of photochemical age. In these calculations a diurnally averaged OH concentration of 3×10^6 molecules cm^{-3} was assumed. Figure 12 depicts these outflow events colored and sized by the photochemical age, with the Mexico City area considered highlighted in the dashed square. The majority of these plume outflows (69%) were intercepted by the DC-8 at radar altitudes ≤2 km. Like Fig. 9, the solid gray squares show VOC point sources sized by their emission values in tons/year. Many of these plume intercepts and/or their back trajectories did not pass near these sources.

Figure 13 shows the resulting CH_2O measurement and model behavior for these Mexico City outflow plumes as a function of photochemical age. Although there is some uncertainty in the photochemical age clock due to a number of causes (assuming a single diurnally averaged OH mixing ratio to represent processing over different time scales, neglecting the effects of dilution on the OH mixing ratios as the plume ages, and

ACPD
11, 9887–9957, 2011

resetting of the photochemical clock as a result of mixing in air masses with different butyl nitrate to butane time histories), Perring et al. (2010) find that the photochemical ages in the first two days are similar to transport times calculated from observed wind speeds. Employing back trajectories for these same Mexico City outflow events, we find similar general agreement: back trajectory times agree with the photochemical age to within ±5 h for butane times between 7.5 and 32.5 h. At shorter times there is ambiguity in the back trajectory determination of air mass origin relative to the butane clock since we do not have a precise location for the start of the butane clock. At longer times the butane times appear to be influenced by local inputs, which reset the butane time to lower values. The discussion which follows will primarily focus on outflow events in the above time range.

Figure 13 displays the fractional enhancement over background for CH_2O measurements, box model values, and CO for various plume age bins. This plot, which is similar to that displayed by Perring et al. (2010) for various species, shows the growth of CH_2O relative to CO as the plume ages. The fractional enhancement (FE) for each is calculated from:

$$FE = (X - X_{bkg})/(X_{inital} - X_{bkg}) \quad (1)$$

Here X represents the binned median concentrations, X_{bkg} are the background concentrations observed at the longest photochemical times over the Gulf ($[CH_2O]_{TDLAS\ meas}$ = 572 pptv, $[CH_2O]_{model}$ = 522 pptv, and [CO] = 113 ppbv), and X_{inital} are the values observed over Mexico City ($[CH_2O]_{TDLAS\ meas}$ = 7793 pptv, $[CH_2O]_{model}$ = 7211 pptv, and [CO] = 600 ppbv). This approach allows one to plot all species on the same vertical axis, with all initial values starting at ∼1 and decaying to 0 with time. The decay in CO here primarily reflects dilution as the plume ages, whereas the CH_2O profiles reflect photochemical loss (reaction with OH and photolysis), dilution, and production as the plume ages. As can be seen, both TDLAS measured and modeled CH_2O show net production relative to CO, which persists as long as ∼1 day downwind. In the case of box model CH_2O, this extra production can only arise from CH_2O precursors at the time of measurement. Median CH_2O production percentages from the model are: CH_4

ACPD
11, 9887–9957, 2011

(46%), PAN and higher acetyl peroxy compounds (18%), methanol (8%), MHP (7%) and ethene (6%) for these air masses. All other precursor contributions are less than 2%. The binned TDLAS CH_2O observations, which are higher than both the modeled values and CO dilution, reflect additional production of CH_2O in the aging outflow plume that is not accounted by the above precursors in the box model. This additional production lasts for times up to ~2 days, and most likely reflects additional CH_2O production from unmeasured primary precursors, including multi-generation daughter species, as well as measured precursors that are not in steady-state with measured values from the DC-8. Biomass burning fire plumes, which have been noted in various Mexico City studies and could have an influence on such outflow plumes, do not play a significant role in the outflow events of Fig. 13. According to Kleinman et al. (2008), air masses have minimal forest fire influence for CH_3CN (ppbv) $<0.2 + 0.4 \times 10^{-3} \times$ [CO] (ppbv). For the present outflow events, 91% of the air masses have lower CH_3CN mixing ratios than this.

To examine whether or not longer lived measured CH_2O-precursors could be responsible for the behavior shown in Fig. 13 during Mexico City outflow events, we employ the same Lagrangian-steady state analysis used in generating Fig. 11b. Here a Lagrangian Mexico City outflow plume (starting at noon) was simulated using input concentrations from the daytime mean measurements shown in Table 2 of Apel et al. (2010) along with NO_x injections of 20 ppbv and O_3 held constant at 56 ppbv. The steady state box model sampled a continuously diluting Lagrangian plume at various times along the simulation. A dilution rate of $k_d = 2.78 \times 10^{-5}\ s^{-1}$ (10 h CO lifetime) was estimated from the CO decay in Fig. 13 and this was used in the following relationship to arrive at diluted Lagrangian mixing ratios at every time step:

$$X = X_{bkg} + (X - X_{bkg}) e^{-(time * k_d)} \quad (2)$$

As in Eq. (1), X_{bkg} is the background concentration observed at the longest photochemical time (photochemical lifetimes >40 h) over the Gulf and X represents the concentration of species X resulting from dilution and photochemistry at each time step. Figure 14a shows the ratio of the Lagrangian to steady state box model (red line with

ACPD
11, 9887–9957, 2011

points) as a proxy of the measurement to steady-state box model relationship averaged over various outflow times. This plot indeed reveals an additional production of CH_2O that is not captured by the steady state model of about 20% for time periods as long as 40–50 h after injection. The species responsible for this include: higher aldehydes like acetaldehyde and higher peroxides, which are produced in large amounts at the beginning of the run and decay away much more slowly than CH_2O. Thus, the DSS modeling approach will underestimate the calculation of these species, which leads to the underestimation of CH_2O. It is interesting to note that this additional 20% of CH_2O production is consistent with many of the geographic flight segment ratios shown in Fig. 9, which show averaged segment measurement/box model ratios around 1.2.

However, this additional production only accounts for about 1/3 of the maximum additional CH_2O suggested by the measurements and does not capture the shape of the measurement-box model discrepancy as further shown by the box and whisker plots in Fig. 14a. Here measurement/box model ratios in 5-h butane time bins are plotted as box and whiskers with median ratios highlighted by horizontal lines with blue points and fit using a 4-term polynomial (blue curve). This plot shows enhanced production of CH_2O with plume age, which reaches a maximum between ~13 and 28 h. Here ratios and differences between measurements and the simple steady state box model are as high as 1.7 and 908 pptv, respectively. Even after accounting for such longer-lived precursors in the Lagrangian model approach, Fig. 14a reveals residual missing CH_2O sources in the Mexico City outflow plume, resulting in discrepancies in the 500 to 700-pptv range.

An analogous calculation was carried out using the online Leeds Master Chemical Mechanism (MCM version 3.1) to assess the effects of additional CH_2O production from both measured hydrocarbons and unmeasured hydrocarbons via explicit chemistry involved in multi-generational production mechanisms. Details regarding the MCM can be found at http://mcm.leeds.ac.uk/MCM, and is further described by Jenkin et al. (1997, 2003), Saunders et al. (2003), and Bloss et al. (2005). In contrast to the more limited suite of NMHCs available on the airborne platforms for box model calculations,

ACPD
11, 9887–9957, 2011

the MCM utilizes a more comprehensive suite of observations from one of the fully instrumented Mexico City sampling sites at T_0. As indicated in Appendix Table A3, starting concentrations for the MCM runs were in most cases derived from 24-h median mixing ratios measured at T_0 by the Blake group at the University of California, Irvine. In some cases close-in measurements from the C-130, the DC-8, or their averages were employed and these were scaled to T_0 values using similar reacting compounds. In all cases where measurements were employed, the "Model Input Designator" column of Appendix Table A3 lists a 1 or 2 designation. A 1 designates that the MCM was initialized using T_0 measurements of that species in the manner just described and that particular species was also explicitly incorporated in the NASA Langley box model using DC-8 observations. A 2 in this column indicates the same MCM source but the NASA Langley box model did not explicitly incorporate that species as an input. A 3 in this column designates unmeasured species in both models where the MCM input mixing ratio was estimated by various methods. In some cases the estimation was from a fit of measured values versus carbon number for the same compound class as the unknown. In other cases estimations were based on the concentrations of similar reacting compounds. These designations were designed to elucidate the potentially important NMHC species that should be measured in future airborne campaigns when studying CH_2O production.

The MCM explicitly follows the products from the degradation of 124 VOCs by OH, O_3, and NO_3. Photolysis of relevant species (e.g. aldehydes) is also explicitly calculated. The mechanism produces a variety of free radical species (peroxy, oxy, and Criegee) that interact with each other and with the other oxidants. This leads to the production of many species, some of which have primary emissions (simple alcohols, aldehydes and ketones), but also those which are only formed in the atmosphere via multistep processes (multifunctional carbonyls, nitrates, peroxy nitrates, hydroperoxides, and carboxylic acids). While not all reactions of these species have been directly measured in the laboratory, the MCM makes use of available data to define rules to construct kinetic and mechanistic details for all species. In order to keep the mechanism

ACPD
11, 9887–9957, 2011

to a manageable size, a few simplifications are made. Products from the attack of OH on many of the VOC are ignored when the channel has a low probability of occurrence. Permutation reactions of a given RO_2 radical are represented by a single parameterized reaction. Other minor processes are ignored if it is assessed that their contribution to the degradation of the VOC is relatively unimportant. As implemented, the mechanism has more than 13000 reactions and more than 4400 non-radical species. In addition, there are nearly 1000 peroxy radical species and more than 1000 alkoxy radical species. There are 290 CH_2O source reactions and 4 loss reactions. As can be seen by the input concentrations in Appendix Table A3, there is a large potential for significant CH_2O production from secondary species that are unconstrained by aircraft observations. Among these are multifunctional species such as those generated from the attack of OH on alkenes (hydroxyl-carbonyls), hydroperoxides produced from RO_2 reaction with HO_2, and PAN-like species from substituted peroxy radical reactions with NO_2. Estimation of the potential importance of oxidation of these species to produce CH_2O is the reason for employing the MCM tool.

The same dilution rate of $k_d = 2.78 \times 10^{-5}\,s^{-1}$ was used in these calculations and this resulted in time dependent CH_2O mixing ratios in 15-min time intervals for 4 different starting times between 00:00 and 18:00 h. Rather than comparing MCM calculations directly with measured CH_2O mixing ratios, which in addition to dilution, input values and comprehensive chemistry depends upon accurate knowledge of the 3-D wind fields, we are more interested here in the MCM comparisons between runs using all species and those that were explicitly measured and employed in the NASA box model. Such a comparison immediately highlights differences that could potentially be due to unmeasured species and/or multi-generation hydrocarbon oxidation processing. This was implemented using the MCM by calculating the steady state CH_2O mixing ratios at each 15-min time step using instantaneous CH_2O production and loss terms in two different ways: one where the calculations were restricted to gas phase species measured and also explicitly incorporated in the NASA Langley box model using DC-8 observations, SS (1), and one where these steady state calculations were allowed to

ACPD
11, 9887–9957, 2011

use the full suite of species in the MCM, SS (1,2,3), including multi-generation species not measured during the campaign. The numbers in parentheses represent the Model Input Designations of Appendix Table A3, as discussed previously. The resulting ratios of CH_2O from the MCM to steady state, MCM/SS (1) and MCM/SS (1,2,3), were determined at each 15-min time step. These ratios, like the Lagrangian to steady state ratios discussed above represent another proxy for the measurement/steady-state box model relationship for various outflow times. Ratios near 1 support the validity of the steady state assumption and little or no missing chemistry in the steady state calculations relative to the full MCM run. High ratios on the other hand further suggest the influence of missing chemistry. These calculations include the fact that some species originated from different sources where the Model Input Designations changed with transport time.

The results of the various calculations were averaged for daytime periods (when observations were made) over all starting times at each reaction time step to arrive at a single median ratio (MCM/SS) at each time step. These in turn were further averaged into 5-h bins to match those in Fig. 14a. The median bin ratio (MCM/SS) is plotted in Fig. 14b by the gray lines and points for the two different steady state model conditions. The upper gray profile, MCM/SS (1), is a surrogate for that expected from simple measurement/NASA Langley box model ratios while the lower profile simulates that expected without the complication of limited observational input (i.e., the lower gray curve should match the red curve). The difference between the two gray profiles represents the influence of unmeasured and multi-generation CH_2O formation.

The lower gray curve yields ratios that are essentially equivalent with the red curve (Lagrangian to steady state box model ratio) for time periods from ~15 to 35 h, which primarily indicates the nearly identical influence of non-steady state conditions in the two models, despite the fact that different hydrocarbon mixtures are included in the two comparisons. At longer and shorter processing times such different mixtures invariably influence the two comparisons, and this is most noticeable by the completely different shapes of the two comparison ratios. More importantly, Fig. 14b shows the comparison

ACPD
11, 9887–9957, 2011

using the same limited input dataset. Here the blue profile, which is the polynomial fit of the binned median measurement/NASA box model ratios, and the upper gray profile (polynomial fit of MCM/SS(1)) have the same shape and the same broad maximum between 18 and 22 h. In this period, the blue and upper gray profiles have values of 1.50 and 1.63, respectively. Ignoring the effects of dilution in these calculations changes the results by less than 1%.

The same MCM runs that produced the upper gray profile was further examined to identify the major species responsible for producing the missing CH_2O not accounted for in steady-state calculations using measured species on the NASA DC-8. Seven major species were identified, and their dependence on transport time is shown in Fig. 14c using the same format as Fig. 14a, b. This figure only includes the reactive intermediates that produce CH_2O and not the starting parent species for which the MCM was initialized. As can be seen, the 7 major missing CH_2O precursors are multiply-substituted second-and higher-generational products, with the largest contribution in all cases from methylglyoxal. In many cases these 7 species do not add up to the polynomial fit of the sum, and these differences represent the many much smaller contributions not included in this figure. In the 15 to 25 h bin ranges, which shows the largest measurement/model discrepancies, ~50% to 60% of the missing CH_2O source originates from methylglyoxal.

The above results imply that steady-state box models employing lumped mechanisms are not sufficient to adequately describe the chemistry that occurs in a complex mixture of hydrocarbons such as that found in the outflow of Mexico City. This is particular true when modeling CH_2O, but also leads to systematic differences for HO_x free radicals (Cantrell et al., 2011). As might be expected, detailed modeling of HO_2 using a similar MCM approach as well as observations are larger than those estimated employing simpler mechanisms because of additional HO_x sources from secondary species. The transport time dependent shapes are similar to that for CH_2O (e.g. Fig. 14b). The presence of such secondary species, furthermore, produces model overestimations in OH employing simple lumped mechanisms since these unaccounted for species are

ACPD
11, 9887–9957, 2011

responsible for additional loss of OH. The details of these findings can be found in Cantrell et al. (2011). It might be possible to extend the steady-state model lumped mechanism to include the effects of these unmeasured and multigenerational species, but that is beyond the scope of this study.

7 Summary and conclusions

A detailed investigation of CH_2O measurements acquired by tunable diode laser absorption spectroscopy and steady state box model calculations using data from the INTEX-B campaign in 2006 reveals for the first time the presence of additional factors that must be taken into account when carrying out such comparisons in the boundary and/or within ~2 days from very large emission sources such as those from megacities. Detailed comparisons indicate large discrepancies, primarily in the 0–2 km (radar altitude) boundary layer, that can neither be explained by: timing errors between measurements and model inputs; combined measurement and box model uncertainty limits; errors in kinetic rate constants and branching ratios; and systematic measurement interferences.

Close to large emission sources of fast reacting alkenes like ethene, measurement-steady- state box model CH_2O comparisons need to take into account processing times in order for such comparisons to make sense. In this study using processing times based on the ratio of 2-butyl nitrate to butane employing measured OH mixing ratios, measurement/steady-state box model ratios are in reasonable agreement out to processing times of ~4 to 6 h only when this is taken into account. Depending upon the exact processing time and lifetimes of CH_2O and the alkene, one can expect model overestimations (factor of ~2), underestimations (factor of ~1.6), or exact agreement with measurements.

This analysis further shows that at longer processing times during Mexico City outflow events, binned median measurement/steady state box model ratios indicate influences from non-steady-state conditions. The ratios show discrepancies as large as 1.7

ACPD
11, 9887–9957, 2011

and 908 pptv for the binned ratios and differences, respectively, for processing times of 10–30 h. Approximately one-third of these discrepancies can be accounted for using an analysis where Lagrangian outflow model calculations, employing typical VOC mixing ratios observed over Mexico City, are sampled by the steady-state box model. Lagrangian/box model ratios up to 1.2 were observed for up to 40 – 50 h in this analysis. Aldehydes like acetaldehyde and higher peroxides, which are produced in large amounts at the beginning of the run and decay away much more slowly than CH_2O, are responsible for this ~20% non-steady state discrepancy. Such a value is consistent with discrepancies observed for many of the geographically averaged flight segments over the Gulf in the boundary layer. Further analysis using the Leeds Master Chemical Mechanism to simulate the full suite of chemical reactions using both measured NMHCs and an estimate of a mix of unmeasured hydrocarbons during the INTEX-B study indicates that unmeasured VOCs, including those from multi-generation oxidation processes, have the potential to influence CH_2O concentrations for up to two days of processing. The maximum effect occurs at processing times between 18 and 22 h, with the largest contribution coming from methylglyoxal, which is neither measured nor explicitly included in steady-state box model calculations.

Although simplified steady-state box model calculations accurately simulate CH_2O observations in many cases, we have presented in this study a possible scenario by which multi-generation CH_2O production can explain observed and calculated CH_2O mixing ratios outside immediate emission regions. This, together with the other aforementioned steady-state issues, further suggest that unless all these additional factors are considered, one should not expect agreement between measured and simplified steady-state box model CH_2O calculations to better than a factor of ~1.7 (500 to 900 pptv differences) from airmasses several days old that have been influenced by very large hydrocarbon emission sources, such as those from megacities. Although it is hard to state with certainty if these causes were also responsible for the boundary layer discrepancies we have observed in certain locations in other studies and observed here in the boundary layer over the Gulf of Mexico, Mexico, and over parts of

ACPD
11, 9887–9957, 2011

the United States, these must be strongly considered as likely possibilities. The various modeling runs highlight the potential importance of various dicarbonyls and hydroxycarbonyls in generating CH_2O about two days downwind of large emission sources and that future airborne CH_2O measurement-box model comparisons should include measurements of these species, particularly methylglyoxal and 3-hyroxypropanal. Efforts are currently underway to identify the starting parent species for the various reactive intermediates shown in Fig. 14c, and this will be the subject of a future publication.

The results of this study must also be considered when apportioning CH_2O into primary and secondary production sources for effective ozone control strategies, as exemplified by Garcia et al. (2006) and Rappenglück et al. (2010 and reference therein). The additional significant 1 to 2-day old CH_2O production we hypothesize here could also be responsible for a large part of the "residual unaccounted CH_2O" deduced from such studies, particularly if the outflow re-circulates over the source region. In these studies such CH_2O represents the amount that could neither be assigned to primary or secondary production sources. Over Mexico City in the spring of 2003, Garcia et al. (2006) deduced that up to 21% of the observed CH_2O (or 2 ppbv) falls into this category, and pointed out that such "unaccounted" CH_2O tends to correlate with higher temperatures and higher ozone in the metropolitan area. The results of the present study add independent support to this conclusion, and indicate that such "residual CH_2O" indeed falls within the secondary production category.

Appendix A

Overview of measurement and box model approaches and uncertainty analysis

A detailed discussion of the TDLAS employed in this work can be found in Fried et al. (2008a, b) and only a very brief overview is presented here. The present instrument is essentially the same as that employed during the INTEX-NA study but with a number of enhancements to the optical system to improve mechanical stability, and

ACPD
11, 9887–9957, 2011

hence, measurement performance. As previously discussed, CH_2O is measured via absorption spectroscopy using a liquid nitrogen cooled tunable lead-salt diode laser to selectively probe a moderately strong and isolated CH_2O absorption feature at 3.53-μm (2831.6417 cm^{-1}) employing a multipass Herriott sampling cell (optical pathlength of 100-m). Ambient measurements were acquired in 1-s increments over time periods ranging from 30 to 120 s, and this was followed by 15 s of background zero air acquisition, obtained by overflowing the inlet with zero air using a commercial Aadco™ zero air generation system to remove CH_2O from the sample stream. During most of the INTEX-B first phase, the ambient mixing ratios were sufficiently high compared to backgrounds that ambient acquisition periods as long as 60 to 120 s were possible before the acquisition of a new background was required. During the second phase over the Pacific, the lower ambient CH_2O levels required more frequent background acquisitions every 30 s. In all cases, the time-weighted average of the background spectra surrounding each ambient period was subtracted point-by-point from each ambient 1 s spectrum, and the resultant spectra were fit to a background-subtracted reference spectrum. The latter was obtained by introducing a high concentration (~8 ppbv) CH_2O calibration mixture from a permeation system in zero air approximately every hour. Further details regarding these calibrations, the inlet, typical operating conditions, data handling and fitting, zero air background subtraction, and assessments of measurement accuracy and limits of detection, can be found in Fried et al. (2008a) and references therein.

Enhanced measurement performance was achieved in this study by mechanical stabilizing three critical system optical components. The first involved the Herriott cell. Roller et al. (2006) discussed a clamping arrangement on the Herriott cell to eliminate changes in mirror pitch and separation during aircraft maneuvers. We further improved on this design. We also mechanically stabilized the first off-axis parabolic (OAP) mirror mount used in collecting and collimating the diode laser radiation. This was accomplished using a clamp to provide continuous downward pressure to the OAP mount and translation stages. Prior to this, even small vertical aircraft accelerations moved

ACPD
11, 9887–9957, 2011

the optical beam, and given the large magnification of this first mirror (~75), such small movements resulted in large beam movements into and out of the Herriott cell, significantly degrading system performance. The cell input/output mirror stage was also mechanically stabilized in the same fashion. All three actions led to improved performance.

As discussed by Fried et al. (2008a), the 2831.6 cm^{-1} CH_2O line is free from all known spectroscopic interferences with the exception of methanol. Extensive laboratory tests indicate that with proper choice of fitting windows, this interference can be reduced to 0.3% in the present TDLAS system (i.e., an error in the retrieved CH_2O mixing ratio of +0.3% times the ambient methanol mixing ratio). The results of the present study, however, were not corrected for this small interference since ambient measurements of methanol on the DC-8 were only available from one of the airborne instruments (the NASA Ames PANIK instrument) less than 50% of the time when CH_2O measurements and box model values were compared. This small positive measurement bias only has a minimal effect on the boundary layer results; when methanol data were available for correction, the median CH_2O (measurement-model) difference only changed by 47 pptv for all boundary layer comparisons during the 1st phase. This is at least an order of magnitude smaller than observed differences.

Box model simulations were carried out employing the NASA Langley time dependent photochemical box model (Crawford et al., 1999; Olson et al., 2001, 2006) with rate constants generally those recommended by Sander et al. (2006) and Atkinson et al. (2006). The parameterization for near-IR photolysis of HNO_4 as described in Roehl et al. (2002) is included. NMHC chemistry is originally based on the lumped scheme in Lurmann et al. (1986), with appropriate adjustments to chemistry as discussed in the appendix of Crawford et al. (1999). As discussed in Fried et al. (2008a), the model calculates for each set of measurements the associated self-consistent diurnal profile of radical and other computed species determined from the constraint of long-lived precursors to measured concentrations. Computed radical concentrations at the same point in time as the measurement are then used as the instantaneous model results.

ACPD
11, 9887–9957, 2011

The hydrocarbon (HC) sampling time base, which represents the time duration in filling each hydrocarbon canister, was used in these calculations, as discussed previously. The average canister fill duration was 70 s. The minimum set of input constraints includes observations of O_3, CO, NO, nonmethane hydrocarbons (NMHCs), acetone, MEK, methanol, ethanol, temperature, H_2O (dew/frost point), pressure, photolysis frequencies, and when available, measurements of H_2O_2, HNO_3, and PAN. Ketones, alcohols, and NMHCs are filled by interpolation or scaling to CO when measurements are unavailable. A further restricted dataset was derived where measurements of MHP were available to constrain the model, where the CH_2O measurements comprised at least 50% of the HC time base, and where the measurements were uniformly distributed over this time base. Depositional loss of CH_2O and other soluble species was invoked below 2 km at a constant value of 1.0×10^{-5} s^{-1} (1.2 cm s^{-1} deposition velocity).

The limits of detection (LOD, 2σ level) for the 1-min TDLAS results discussed here were independently determined for each flight based upon the median replication precision of 1-s ambient measurements over 30-s to 1-min time intervals. Laboratory tests have shown that the instrument precision generally improved by the square-root of the averaging time up to averaging periods of 30 to 60-s. Equivalent 1-min precisions were determined from the 1-s precisions by dividing these results by the square-root of 30 in all cases (even for 60-s of averaging, just to be conservative). Since ambient variability can contribute to the signal variability, these LOD estimates are conservative upper limits. Using these procedures we arrive at 1-min (2σ) measurement LODs ranging between 39 pptv to 59 pptv for the entire mission with a median value of 47 pptv for all flights combined. These values were further confirmed on a number of occasions from the replicate precision of 1-min ambient measurements carried out over at least 5-min when the ambient CH_2O mixing ratios were low and stable. A total systematic error (2σ level) of 13% was estimated from the quadrature addition of various individual uncertainties involving flow and flow dilution uncertainties, and uncertainties in the CH_2O permeation rate and calibration factors over the course of the mission.

ACPD
11, 9887–9957, 2011

The uncertainty in box model predictions of CH_2O and other radicals include a component due to uncertainties in the measurement of constrained species (*model constraint uncertainty*), and a component due to uncertainties in kinetic and photolytic rates (*model kinetic uncertainty*). The *model constraint uncertainty* was determined for every modeled point on the hydrocarbon time base using a sensitivity approach similar to Frost et al. (2002). The box model was run 11 times for every data point; each time one of the 11 constraints considered was increased by its given 1σ measurement uncertainty. The considered constraints include O_3, CO, NO, acetone, alcohols, ethene, higher alkenes, alkanes, isoprene, and MHP. The absolute value of the relative change in modeled CH_2O then represents the 1σ uncertainty in calculated CH_2O for that given constraint. The individual uncertainties for each constraint were combined in quadrature for a total *model constraint uncertainty*. While the given uncertainties in measurements of the model constraints include both random and systematic errors, we consider the propagated uncertainty to be largely random in nature, and henceforth all mention of model uncertainty refers to such *model constraint uncertainty*, unless stated otherwise. For conditions over the remote Pacific, the *model constraint uncertainty* for CH_2O (converted to 2σ) ranges from 22–34% throughout the altitude regime considered. Values over the continental US and Mexico range from 8–35%. The combined random measurement and *model constraint uncertainty* (2σ level) for each altitude range bin was then estimated by quadrature addition of the measurement LOD with the *model constraint uncertainty*, and the average value for each altitude bin was determined.

In addition, the *model kinetic uncertainty* was calculated using a Monte Carlo approach. Median environmental and chemical conditions were found for various altitude levels for the US/Mexico portion and for the Pacific portion of INTEX-B. For each set of input conditions, the *model kinetic uncertainty* was calculated by running 2500 simulations whereby each of 105 model kinetic reaction rates and 16 photolytic rates was randomly and independently varied within its referenced 1σ uncertainty. The standard deviations of the resulting range of predictions can be used to define the

ACPD
11, 9887–9957, 2011

model kinetic uncertainty for various predicted radical species. While this component of model uncertainty is generally considered systematic, it can vary, depending upon changes in the chemical and environmental regimes. This component of uncertainty (2σ) was calculated to range from 50%–62% (boundary layer – high altitudes, Pacific) and 34%–68% (Boundary layer – high altitudes, Houston) for CH_2O during INTEX-B.

Appendix B

Overview of past TDLAS comparisons with other techniques

Comparisons of an earlier version of the present airborne system employing a different CH_2O absorption feature produced results that agreed with long-path ultraviolet/visible DOAS results to within 5% when both instruments sampled the same air mass unperturbed by local anthropogenic and meteorological influences (Harder et al., 1997). An earlier version of the present airborne TDLAS system (employing the same 2831.6 cm^{-1} absorption line) was also compared with three continuous non-spectroscopic methods, including a coil Hantzsch system, during an extensive ground-based CH_2O intercomparison study discussed by Gilpin et al. (1997). After correcting for calibration differences using a common standard provided by the TDLAS system, all four instruments retrieved equivalent ambient CH_2O mixing ratios within ±18%, and two of the non-spectroscopic instruments were within 4% of the TDLAS retrievals. An earlier version of the present TDLAS system was also compared with one of the non-spectroscopic methods in the Gilpin et al. study onboard a NOAA aircraft during the 1997 NARE study (Fried et al., 2002). A bivariant least squares fit of this instrument versus the TDLAS for 665 overlapping 5-min time coincident intervals resulted in a slope of 0.987 and intercept of 0.027 ppbv for mixing ratios up to 2 ppbv. Furthermore, the two instruments measured identical CH_2O mixing ratios to within ~0.1 ppbv, and more typically within 0.08 ppbv, in 3 altitude bins up to ~8 km over the 0–0.8 ppbv range. Finally, Wert et al. (2003) compared airborne CH_2O measurements using an

ACPD
11, 9887–9957, 2011

earlier version of the present TDLAS system with a ground based DOAS system operated by Stutz during the 2000 Texas Air Quality Study. During aircraft overflights (40–60 m above the ground) of the DOAS sampling site when three different DOAS paths spanning altitudes from 2 to 50 m above ground indicated uniform mixing, the agreement between the two techniques was within 5%.

Appendix C

Overview of present airborne TDL comparisons with ground based measurements

There were nine different time periods when either the DC-8 or the C-130 passed very close to ground sampling sites over Mexico City and when ground-based CH_2O measurements were also acquired employing a Hantzsch system operated by Junkermann's research group (see Hak et al., 2005 for a description of this instrument) and/or a DOAS instrument operated by Volkamer's group). Appendix Table A1 tabulates the pertinent information regarding the two overpasses by the DC-8 while Appendix Tables A2a and A2b tabulate C-130 overpasses. Numerous diagnostics from ground, airborne, and balloon-sounding systems indicated uniform sampled air between the airborne and ground-based measurements. These diagnostics include: airborne aerosol measurements using the NASA Langley lidar system on the DC-8 (Browell et al., 2003) and the NCAR SABL Lidar system on the C-130, a ground-based micro-pulsed lidar system located at T_1, 915 MHz radar wind profilers operated by Phillips and Knupp at the University of Alabama (see Cronce et al., 2007) and a Ceilometer backscatter profiler, and balloon soundings of constant potential temperature.

The C-130 overpasses close to the T_0, T_1, and T_2 ground-sampling sites are listed in Appendix Tables A2a and A2b. Appendix Table A2a lists time periods when ground-based CH_2O measurements were acquired employing the Hantzsch system operated by Junkermann's research group and Appendix Table A2b lists time periods when the

ACPD
11, 9887–9957, 2011

University of Colorado's MAX-DOAS system acquired vertical column measurements of CH_2O. When used with boundary layer height estimates from Lidar and/or wind profiler measurements and the assumption of vertical uniformity, the MAX-DOAS column measurements can be used to derive CH_2O mixing ratios for comparisons with the C-130 measurements. Since boundary layer height estimates may be uncertain in some cases, vertical column derived CH_2O mixing ratios were corrected by the ratio of DOAS derived NO_2-to C-130 in situ measurements of NO_2 by Weinheimer's group. These corrections assume that the lifetimes of both gases are longer than vertical mixing times and both gases have similar vertical distributions, i.e., that mixing (or lack thereof) does not introduce new sources of one gas relative to the other. During times of the DC-8 overpasses mixing is well developed, and gradients are expected to be small. DOAS derived NO_2-to C-130 measurement ratios were within 11% of the same ratios for CH_2O, suggesting the above assumptions should be valid. Although the C-130 and DOAS measurements times indicated in Table A2b were not precisely time coincident, the time differences were within ~0.5 to 1.5 h.

Acknowledgements. The National Center for Atmospheric Research is operated by the University Corporation for Atmospheric Research under the sponsorship of the National Science Foundation. This research was supported by funds from the National Aeronautics and Space Administration's Global Tropospheric Program and by funds from NSF in support of the MIRAGE Study. The authors specifically wish to acknowledge the NASA/University of North Dakota DC-8 staff and crew for all their valuable support and assistance as well as two former members of the NCAR Design and Fabrication Services Facility, Jack Fox and Ken Harris. We also acknowledge Bruce Morley and Gordon Farquharson for the SABL (Scanning Aerosol Backscatter Lidar) aerosol measurements on the C-130 and Dustin Phillips and Kevin Knupp at the University of Alabama in Huntsville for their profiler data. We also acknowledge Thomas Wagner, Ulrich Platt and Luisa Molina for loan of equipment and support in generating the DOAS dataset.

ACPD
11, 9887–9957, 2011

References

Atkinson, R., Baulch, D. L., Cox, R. A., Crowley, J. N., Hampson, R. F., Hynes, R. G., Jenkin, M. E., Rossi, M. J., Troe, J., and IUPAC Subcommittee: Evaluated kinetic and photochemical data for atmospheric chemistry: Volume II - gas phase reactions of organic species, Atmos. Chem. Phys., 6, 3625–4055, doi:10.5194/acp-6-3625-2006, 2006.

Apel, E. C., Emmons, L. K., Karl, T., Flocke, F., Hills, A. J., Madronich, S., Lee-Taylor, J., Fried, A., Weibring, P., Walega, J., Richter, D., Tie, X., Mauldin, L., Campos, T., Weinheimer, A., Knapp, D., Sive, B., Kleinman, L., Springston, S., Zaveri, R., Ortega, J., Voss, P., Blake, D., Baker, A., Warneke, C., Welsh-Bon, D., de Gouw, J., Zheng, J., Zhang, R., Rudolph, J., Junkermann, W., and Riemer, D. D.: Chemical evolution of volatile organic compounds in the outflow of the Mexico City Metropolitan area, Atmos. Chem. Phys., 10, 2353–2375, doi:10.5194/acp-10-2353-2010, 2010.

Bertman, S. B., Roberts, J. M., Parrish, D. D., Buhr, M. P., Goldman, P. D., Kuster, W. C., Fehsenfeld, F. C., Montzka, S. A., and Westberg, H.: Evolution of Alkyl Nitrates with Air-Mass Age, J. Geophys. Res., 100, 22805–22813, 1995.

Bloss, C., Wagner, V., Jenkin, M. E., Volkamer, R., Bloss, W. J., Lee, J. D., Heard, D. E., Wirtz, K., Martin-Reviejo, M., Rea, G., Wenger, J. C., and Pilling, M. J.: Development of a detailed chemical mechanism (MCMv3.1) for the atmospheric oxidation of aromatic hydrocarbons, Atmos. Chem. Phys., 5, 641–664, doi:10.5194/acp-5-641-2005, 2005.

Browell, E. V., Fenn, M. A., Butler, C. F., Grant, W. B., Brackett, V. G., Hair, J. W., Avery, M. A., Newell, R. E., Hu, Y., Fuelberg, H. E., Jacob, D. J., Anderson, B. E., Atlas, E. L., Blake, D. R., Brune, W. H., Dibb, J. E., Fried, A., Heikes, B. G., Sachse, G. W., Sandholm, S. T., Singh, H. B., Talbot, R. W., Vay, S. A., Weber, R. J., and Bartlett, K. B.: Large-Scale Ozone and Aerosol Distributions, Air Mass Characteristics, and Ozone Fluxes Over the Western Pacific Ocean in Late Winter/Early Spring, J. Geophys. Res., 108(D20), 8805, doi:10.1029/2002JD003290, 2003.

Cantrell, C. A., Hornbrook, R. S., Mauldin, R. L., Kociuch, E. J., Eisele, F. L., et al.: Evolution of Photochemical Activity in the Outflow of Mexico City, Atmos. Chem. Phys., in preparation, 2011.

Carlier, P., Hannachi, H., and Mouvier, G.: The chemistry of carbonyl compounds in the atmosphere: A review, Atmos. Environ., 20, 2079–2099, 1986.

Coburn, S., Dix, B., Sinreich, R., and Volkamer, R.: Development and characterization of

ACPD
11, 9887–9957, 2011

the CU ground MAX-DOAS instrument: lowering RMS noise and first measurements of BrO, IO, and CHOCHO near Pensacola, FL, Atmos. Meas. Tech. Discuss., 4, 247–284, doi:10.5194/amtd-4-247-2011, 2011.

Crawford, J., Davis, D., Olson, J., Chen, G., Liu, S., Gregory, G., Barrick, J., Sachse, G., Sandholm, S., Heikes, B., Singh, H., and Blake, D.: Assessment of upper tropospheric HO_x sources over the tropical Pacific based on NASA GTE/PEM data: net effect on HO_x and other photochemical parameters, J. Geophys. Res., 104, 16255–16273, 1999.

Cronce, M., Rauber, R. M., Knupp, K. R., Jewett, B. F., Walters, J. T., and Phillips, D.: Vertical Motions in Precipitation Bands in Three Winter Cyclones, J. Am. Meteorol. Soc., 46, 1523–1543, doi:10.1175/JAM2533.1, 2007.

Dasgupta, P. K., Li, J., Zhang, G., Luke, W. T., McClenny, W. A., Stutz, J., and Fried, A.: Summertime ambient formaldehyde in five U.S. metropolitan areas: Nashville, Atlanta, Houston, Philadelphia, and Tampa, Environ. Sci. Technol., 39, 4767–4783, 2005.

Dusanter, S., Vimal, D., Stevens, P. S., Volkamer, R., Molina, L. T., Baker, A., Meinardi, S., Blake, D., Sheehy, P., Merten, A., Zhang, R., Zheng, J., Fortner, E. C., Junkermann, W., Dubey, M., Rahn, T., Eichinger, B., Lewandowski, P., Prueger, J., and Holder, H.: Measurements of OH and HO2 concentrations during the MCMA-2006 field campaign - Part 2: Model comparison and radical budget, Atmos. Chem. Phys., 9, 6655–6675, doi:10.5194/acp-9-6655-2009, 2009.

Fried, A., Lee, Y.-N., Frost, G., Wert, B., Henry, B., Drummond, J. R., Hubler, G., and Jobson, T.: Airborne CH_2O measurements over the North Atlantic during the 1997 NARE campaign: instrument comparisons and distributions, J. Geophys. Res., 107, 4039, doi:10.1029/2000JD000260, 2002.

Fried, A., Wang, Y., Cantrell, C., Wert, B., Walega, J., Ridley, B., Atlas, E., Shetter, R., Lefer, B., Coffey, M. T., Hannigan, J., Blake, D., Blake, N., Meinardi, S., Talbot, B., Dibb, J., Scheuer, E., Wingenter, O., Snow, J., Heikes, B., and Ehhalt, D.: Tunable Diode Laser Measurements of Formaldehyde During the TOPSE 2000 Study: Distributions, Trends, and Model Comparisons, J. Geophys. Res., 108(D4), 8365, doi:10.1029/2002JD002208, 2003a.

Fried, A., Crawford, J., Olson, J., Walega, J., Potter, W., Wert, B., Jordan, C., Anderson, B., Shetter, R., Lefer, B., Blake, D., Blake, N., Meinardi, S., Heikes, B., O'Sullivan, D., Snow, J., Fuelberg, H., Kiley, C. M., Sandholm, S., Tan, D., Sachse, G., Singh, H., Faloona, I., Harward, C. N., and Carmichael, G. R.: Airborne Tunable Diode Laser Measurements of Formaldehyde During TRACE-P: Distributions and Box-Model Comparisons, J. Geophys.

ACPD
11, 9887–9957, 2011

Res., 108(D20), 8798, doi:10.1029/2003JD003451, 2003b.
Fried, A., Walega, J. G., Olson, J. R., Crawford, J. H., Chen, G., Weibring, P., Richter, D., Roller, C, Tittel, F. K., Heikes, B. G., Snow, J. A., Shen, H., O'Sullivan, D. W., Porter, M., Fuelberg, H., Halland, J., and Millet, D.: Formaldehyde Over North America and the North Atlantic During the Summer 2004 INTEX Campaign: Methods, Observed Distributions, and Measurement-Model Comparisons, J. Geophys. Res., 113, D10302, doi:10.1029/2007JD009185, 2008a.
Fried, A., Olson, J. R., Walega, J. G., Crawford, J. H., Chen, G., Weibring, P., Richter, D., Roller, C., Tittel, F., Porter, M., Fuelberg, H., Halland, J., Bertram, T. H., Cohen, R. C., Pickering, K., Heikes, B. G., Snow, J. A., Shen, H., O'Sullivan, D. W., Brune, W. H., Ren, X., Blake, D. R., Blake, N., Sachse, G., Diskin, G. S., Podolske, J., Vay, S. A., Shetter, R. E., Hall, S. R., Anderson, B. E., Thornhill, L., Clark, A. D., McNaughton, C. S., Singh, H. B., Avery, M. A., Huey, G., Kim, S., and Millet, D. B.: Role of Convection in Redistributing Formaldehyde to the Upper Troposphere Over North America and the North Atlantic During the Summer 2004 INTEX Campaign, J. Geophys. Res., 113, D17306, doi:10.1029/2007JD009760, 2008b.
Frost, G. J., Fried, A., Lee, Y.-N., Wert, B., Henry, B., Drummond, J. R., Evans, M. J., Fehsenfeld, F. C., Goldan, P. D., Holloway, J. S., Hubler, G., Jakoubek, R., Jobson, B. T., Knapp, K., Kuster, W. C., Roberts, J., Rudolph, J., Ryerson, T. B., Stohl, A., Stroud, C., Sueper, D. T., Trainer, M., and Williams, J.: Comparisons of Box Model Calculations and Measurements of Formaldehyde from the 1997 North Atlantic Regional Experiment, J. Geophys. Res., 107(D8), 4060, doi:10.1029/2001JD000896, 2002.
Garcia, A. R., Volkamer, R., Molina, L. T., Molina, M. J., Samuelson, J., Mellqvist, J., Galle, B., Herndon, S. C., and Kolb, C. E.: Separation of emitted and photochemical formaldehyde in Mexico City using a statistical analysis and a new pair of gas-phase tracers, Atmos. Chem. Phys., 6, 4545–4557, doi:10.5194/acp-6-4545-2006, 2006.
Gilpin, T., Apel, E., Fried, A., Wert, B., Calvert, J., Genfa, Z., Dasgupta, P., Harder, J. W., Heikes, B., Hopkins, B., Westberg, H., Kleindienst, T., Lee, Y.-N., Zhou, X., Lonneman, W., and Sewell, S.: Intercomparison of Six Ambient [CH_2O] Measurement Techniques, J. Geophys. Res., 102(D17), 21161–21188, 1997.
Hak, C., Pundt, I., Trick, S., Kern, C., Platt, U., Dommen, J., Ordóñez, C., Prévôt, A. S. H., Junkermann, W., Astorga-Lloréns, C., Larsen, B. R., Mellqvist, J., Strandberg, A., Yu, Y., Galle, B., Kleffmann, J., Lörzer, J. C., Braathen, G. O., and Volkamer, R.: Intercomparison of four different in-situ techniques for ambient formaldehyde measurements in urban air, Atmos. Chem. Phys., 5, 2881–2900, doi:10.5194/acp-5-2881-2005, 2005.

ACPD
11, 9887–9957, 2011

Herndon, S. C., Jayne, J. T., Zahniser, M. S., Worsnop, D. R., Knighton, B., Alwine, E., Lamb, B. K., Zavala, M., Nelson, D. D., McManus, J. B., Shorter, J. H., Canagaratna, M. R., Onasch, T. B., and Kolb, C. E.: Characterization of Urban Pollutant Emission Fluxes and Ambient Concentration Distributions using a Mobile Laboratory with Rapid Response Instrumentation, Faraday Discuss., 130, 327–339, 2005.

Harder, J. W., Fried, A., Sewell, S., and Henry, B.: Comparison of tunable diode laser and long-path ultraviolet/visible spectroscopic measurements of ambient formaldehyde concentrations during the 1993 OH Photochemistry Experiment, J. Geophys. Res., 102, 6267–6282, 1997.

Jenkin, M. E., Saunders, S. M., and Pilling, M. J.: The Tropospheric Degradation of Volatile Organic Compounds: A Protocol for Mechanism Development, Atmos. Environ., 31(1), 81–104, 1997.

Jenkin, M. E., Saunders, S. M., Wagner, V., and Pilling, M. J.: Protocol for the development of the Master Chemical Mechanism, MCM v3 (Part B): tropospheric degradation of aromatic volatile organic compounds, Atmos. Chem. Phys., 3, 181–193, doi:10.5194/acp-3-181-2003, 2003.

Junkermann, W.: On the distribution of formaldehyde in the western Po-Valley, Italy, during FORMAT 2002/2003, Atmos. Chem. Phys., 9, 9187–9196, doi:10.5194/acp-9-9187-2009, 2009.

Kleb, M. M., Chen, G., Crawford, J. H., Flocke, F. M., and Brown, C. C.: An overview of measurement comparisons from the INTEX-B/MILAGRO airborne field campaign, Atmos. Meas. Tech., 4, 9–27, doi:10.5194/amt-4-9-2011, 2011.

Kleinman, L. I., Springston, S. R., Daum, P. H., Lee, Y.-N., Nunnermacker, L. J., Senum, G. I., Wang, J., Weinstein-Lloyd, J., Alexander, M. L., Hubbe, J., Ortega, J., Canagaratna, M. R., and Jayne, J.: The time evolution of aerosol composition over the Mexico City plateau, Atmos. Chem. Phys., 8, 1559–1575, doi:10.5194/acp-8-1559-2008, 2008.

Kormann, R., Fischer, H., de Reus, M., Lawrence, M., Brühl, Ch., von Kuhlmann, R., Holzinger, R., Williams, J., Lelieveld, J., Warneke, C., de Gouw, J., Heland, J., Ziereis, H., and Schlager, H.: Formaldehyde over the eastern Mediterranean during MINOS: Comparison of airborne in-situ measurements with 3D-model results, Atmos. Chem. Phys., 3, 851–861, doi:10.5194/acp-3-851-2003, 2003.

Lee, M., Heikes, B. G., Jacob, D. J., Sachse, G., and Anderson, B.: Hydrogen peroxide, organic hydroperoxide, and formaldehyde as primary pollutants from biomass burning, J. Geophys. Res., 102, 1301–1309, 1997.

ACPD
11, 9887–9957, 2011

Lei, W., Zavala, M., de Foy, B., Volkamer, R., and Molina, L. T.: Characterizing ozone production and response under different meteorological conditions in Mexico City, Atmos. Chem. Phys., 8, 7571–7581, doi:10.5194/acp-8-7571-2008, 2008.

Lei, W., Zavala, M., de Foy, B., Volkamer, R., Molina, M. J., and Molina, L. T.: Impact of Primary Formaldehyde on Air Pollution in the Mexico City Metropolitan Area, 9, 2607–2618, 2009.

Lurmann, F. W., Lloyd, A. C., and Atkinson, R.: A Chemical Mechanism for Use in Long-Range Transport/Acid Deposition Computer Modeling, J. Geophys. Res., 91(D10), 10905–10936, 1986.

Mao, J., Ren, X., Brune, W. H., Olson, J. R., Crawford, J. H., Fried, A., Huey, L. G., Cohen, R. C., Heikes, B., Singh, H. B., Blake, D. R., Sachse, G. W., Diskin, G. S., Hall, S. R., and Shetter, R. E.: Airborne measurement of OH reactivity during INTEX-B, Atmos. Chem. Phys., 9, 163–173, doi:10.5194/acp-9-163-2009, 2009.

Martin, B. D., Fuelberg, H. E., Blake, N. J., Crawford, J. H., Logan, J. A., Blake, D. R., and Sachse, G. W.: Long range transport of Asian outflow to the equatorial Pacific, J. Geophys. Res., 108(D2), 8322, doi:10.1029/2001JD001418, 2003.

Molina, L. T., Madronich, S., Gaffney, J. S., Apel, E., de Foy, B., Fast, J., Ferrare, R., Herndon, S., Jimenez, J. L., Lamb, B., Osornio-Vargas, A. R., Russell, P., Schauer, J. J., Stevens, P. S., Volkamer, R., and Zavala, M.: An overview of the MILAGRO 2006 Campaign: Mexico City emissions and their transport and transformation, Atmos. Chem. Phys., 10, 8697–8760, doi:10.5194/acp-10-8697-2010, 2010.

Olaguer, E. P., Rappenglück, B., Lefer, B., Stutz, J., Dibb, J., Griffin, R., Brune, W. H., Shauck, M., Buhr, M., Jeffries, H., Vizuete, W., and Pinto, J. P.: Deciphering the Role of Radical Precursors During the Second Texas Air Quality Study, J. Air Waste Manage. Assoc., 59, 1258–1277, 2009.

Olson, J. R., Crawford, J. H., Davis, D. D., Chen, G., Avery, M. A., Barrick, J. D. W., Sachse, G. W., Vay, S. A., Sandholm, S. T., Tan, D., Brune, W. H., Faloona, I. C., Heikes, B. G., Shetter, R. E., Lefer, B. L., Singh, H. B., Talbot, R. W., and Blake, D. R.: Seasonal differences in the photochemistry of the South Pacific: A comparison of observations and model results from PEM-Tropics A and B, J. Geophys. Res., 106, 32749–32766, 2001.

Olson, J. R., Crawford, J. H., Chen, G., Brune, W. H., Faloona, I. C., Tan, D., Harder, H., and Martinez, M.: A Reevaluation of HO_x Observations from NASA Field Campaigns, J. Geophys. Res., 111, D10301, doi:10.1029/2005JD006617, 2006.

Perring, A. E., Bertram, T. H., Farmer, D. K., Wooldridge, P. J., Dibb, J., Blake, N. J., Blake,

ACPD
11, 9887–9957, 2011

D. R., Singh, H. B., Fuelberg, H., Diskin, G., Sachse, G., and Cohen, R. C.: The production and persistence of SRONO2 in the Mexico City plume, Atmos. Chem. Phys., 10, 7215–7229, doi:10.5194/acp-10-7215-2010, 2010.

Rappenglück, B., Dasgupta, P. K., Leuchner, M., Li, Q., and Luke, W.: Formaldehyde and its relation to CO, PAN, and SO_2 in the Houston-Galveston airshed, Atmos. Chem. Phys., 10, 2413–2424, doi:10.5194/acp-10-2413-2010, 2010.

Ren, X., Olson, J. R., Crawford, J. H., Brune, W. H., Mao, J., Long, R. B., Chen, Z., Chen, G., Avery, M. A., Sachse, G. W., Barrick, J. D., Diskin, G. S., Huey, L. G., Fried, A., Cohen, R. C., Heikes, B., Wennberg, P. O., Singh, H. B., Blake, D. R., and Shetter, R. E.: HO_x Chemistry During INTEX-A 2004: Observation, Model Calculation, and Comparison with Previous Studies, J. Geophys. Res., 113, D05310, doi:10.1029/2007JD009166, 2008.

Roehl, C. A., Nizkorodov, S. A., Blake, G. A., and Wennberg, P. O.: Photodissociation of Peroxynitric acid in the Near IR, J. Phys. Chem. A, 106(15), 3766–3772, 2002.

Roller, C., Fried, A., Walega, J., Weibring, P., and Tittel, F.: Advances in Hardware, System Diagnostics Software, and Acquisition Procedures for High Performance Airborne Tunable Diode Laser Measurements of Formaldehyde, Appl. Phys. B, 82, 247–264, 2006.

Sander, S. P., Ravishankara, A. R., Golden, D. M., Kolb, C. E., Kurylo, M. J., Molina, M. J., Moortgat, G. K., Finlayson-Pitts, B. J., Wine, P. H., Huie, R. E., and Orkin, V. L.: Chemical Kinetics and Photochemical Data for Use in Atmospheric Studies Evaluation Number 15, JPL Publication 06-2, 2006.

Saunders, S. M., Jenkin, M. E., Derwent, R. G., and Pilling, M. J.: Protocol for the development of the Master Chemical Mechanism, MCM v3 (Part A): tropospheric degradation of non-aromatic volatile organic compounds, Atmos. Chem. Phys., 3, 161–180, doi:10.5194/acp-3-161-2003, 2003.

Singh, H. B., Brune, W. H., Crawford, J. H., Flocke, F., and Jacob, D. J.: Chemistry and transport of pollution over the Gulf of Mexico and the Pacific: spring 2006 INTEX-B campaign overview and first results, Atmos. Chem. Phys., 9, 2301–2318, doi:10.5194/acp-9-2301-2009, 2009.

Sinreich, R., Coburn, S., Dix, B., and Volkamer, R.: Ship-based detection of glyoxal over the remote tropical Pacific Ocean, Atmos. Chem. Phys., 10, 11359–11371, doi:10.5194/acp-10-11359-2010, 2010.

Volkamer, R., Sheehy, P., Molina, L. T., and Molina, M. J.: Oxidative capacity of the Mexico City atmosphere - Part 1: A radical source perspective, Atmos. Chem. Phys., 10, 6969–6991, doi:10.5194/acp-10-6969-2010, 2010.

ACPD
11, 9887–9957, 2011

Wert, B. P., Trainer, M., Fried, A., Ryerson, T. B., Henry, B., Potter, W., Angevine, W. M., Atlas, E., Donnelly, S. G., Fehsenfeld, F. C., Frost, G. J., Goldan, P. D., Hansel, A., Holloway, J. S., Hubler, G., Kuster, W. C., Nicks Jr., D. K., Neuman, J. A., Parrish, D. D., Schauffler, S., Stutz, J., Sueper, D. T., Wiedinmyer, C., and Wisthaler, A.: Signatures of terminal alkene oxidation in airborne formaldehyde measurements during TexAQS 2000, J. Geophys. Res., 108(D3), 4104, doi:10.1029/2002JD002502, 2003.

ACPD
11, 9887–9957, 2011

Table 1. Radar altitude bin statistics for time coincident TDLAS measurements (Meas) and box model (Model) on hydrocarbon time base during the 1st phase of INTEX-B for the NASA DC-8. All measurement and model results, including (Meas-Model) are in pptv. The difference and ratios were determined from the point-to-point comparisons.

Radar Alt (km)	Median Meas	Median Model	Median (Meas-Model)	Median Meas/Model	*N*
0 to 0.5	1635	1248	258	1.20	120
0.5 to 1	1874	1297	424	1.28	65
1 to 2	1285	909	403	1.47	92
2 to 4	503	459	121	1.35	174
4 to 6	107	111	−26	0.85	86
6 to 8	75	72	−1	0.99	63
8 to 10	44	57	−11	0.77	50
10 to 12	26	39	−23	0.44	21

ACPD
11, 9887–9957, 2011

Table 2. Radar altitude bin statistics for time coincident TDLAS measurements (Meas) and box model (Model) on hydrocarbon time base during the 2nd phase of INTEX-B for the NASA DC-8. All measurement and model results, including (Meas-Model) are in pptv. The difference and ratios were determined from the point-to-point comparisons.

Radar Alt (km)	Median Meas	Median Model	Median (Meas-Model)	Median Meas/Model	*N*
0 to 0.5	298	278	39	1.15	111
0.5 to 1	178	146	10	1.13	33
1 to 2	226	187	1	1.01	74
2 to 4	150	154	−15	0.90	184
4 to 6	60	95	−35	0.58	207
6 to 8	51	72	−28	0.64	188
8 to 10	27	42	−27	0.46	189
10 to 12	35	34	−4	0.88	118

ACPD
11, 9887–9957, 2011

Table A1. DC-8 (TDLAS) and ground-based (Hantzsch) comparisons of ambient CH_2O over Mexico City. The distance is the aircraft distance to the site and the altitude is the height above ground from the aircraft radar. The mixing ratios are in ppbv.

Ground Site	Date/Time (GMT)	Distance (km)	Altitude (km)	$[CH_2O]$ Hantzsch	$[CH_2O]$ TDLAS
Tenago	3/12/06 22:28:01	4	0.32	8.070	7.752
T_1	3/11/06 20:22:34	6.2	0.28	5.440	5.189

ACPD
11, 9887–9957, 2011

Table A2a. C-130 (DFG) and ground-based (Hantzsch) comparisons of ambient CH_2O over Mexico City. The distance is the aircraft distance to the site and the altitude is the height above ground from the aircraft radar. The mixing ratios are in ppbv.

Ground Site	Date/Time (GMT)	Distance (km)	Altitude (km)	[CH_2O] Hantzsch	[CH_2O] DFG
T_0	3/22/06 20:18:00	0.8	0.59	11.270	11.159
T_1	3/22/06 20:27:00	3.1	1.04	6.630	6.730
T_1	3/22/06 20:39:00	3.9	1.66	7.030	6.747
T_1	3/22/06 20:40:00	3.6	1.72	7.070	6.360

ACPD
11, 9887–9957, 2011

Table A2b. C-130 (DFG) and ground-based DOAS comparisons of ambient CH_2O over Mexico City. The distance is the aircraft distance to the site and the altitude is the height above ground from the aircraft radar. The mixing ratios are in ppbv. The assumed boundary layer height (BL) in km is also indicated as well as the DOAS measurement time. The DOAS CH_2O was normalized by the DOAS/C-130 measurements of NO_2 to account for errors in the BL determination.

Ground Site	Date/Time (GMT) Aircraft	Time (GMT) DOAS	Distance (km)	Altitude (km)	$[CH_2O]$ DOAS	$[CH_2O]$ DFG	BL (km)
T_0	3/22/06 20:18:00	19:46:05	0.8	0.59	12.023	11.159	1.63
T_0	3/29/06 20:25:00	19:42:47	0.4	0.57	10.926	10.669	1.50
T_2	3/29/06 19:14:00	20:54:46	2.2	0.64	2.323	2.095	1.06

ACPD
11, 9887–9957, 2011

Table A3. Initial species mixing ratios (pptv unless otherwise indicated) used in MCM runs. The "Source" column indicates how these mixing ratios were determined. In the "Model Input Designator" column a **1** indicates that measurements were used and that the NASA Langley Box Model explicitly incorporates DC-8 measurements of that species as an input. MCM measurements were typically from 24-h median University of California Irvine (UCI) ground-based measurements at T_0 (see Apel et al., 2010) where available, or from aircraft measurements (C-130, DC-8 or their average). A **2** indicates the same MCM measurement source but the NASA Box Model did not explicitly incorporate that species as an input, and a **3** indicates an unmeasured species in both models whose mixing ratio was estimated.

Class	Species/ Parameter	Mixing Ratio	Model Input Designator	Source
Major	Methane	2800 ppbv	1	T0-Blake[a]
	Water	6670 ppmv	1	Outflow average[c]
	Carbon monoxide	1600 ppbv	1	T0-Blake
	Ozone	5 ppbv	1	T0-Kolb[b]
	Hydrogen	550 ppbv		Typical value
NMHC-Alkanes	Ethane	10 000	1	T0-Blake
	Propane	60 000	1	T0-Blake
	i-Butane	12 000	1	T0-Blake
	n-Butane	31 000	1	T0-Blake
	i-Pentane	8000	1	T0-Blake
	neo-Pentane	10	3	Small value estimate
	n-Pentane	5600	1	T0-Blake
	2,2-Dimethylbutane	730	2	T0-Blake
	2,3-Dimethylbutane	3700	2	T0-Blake
	2-Methylpentane	3400	1	T0-Blake
	3-Methylpentane	2500	1	T0-Blake
	Cyclohexane	400	2	T0-Apel
	n-Hexane	3800	1	T0-Blake
	2-methylhexane	700	3	fit of Alkanes vs. #C[f]
	3-methylhexane	700	3	fit of Alkanes vs. #C[f]
	n-Heptane	760	1	T0-Blake
	n-Octane	270	2	T0-Blake
	n-Nonane	190	2	T0-Blake
	n-Decane (ND)	290	2	T0-Blake
	Undecane (UD)	100	3	fit (UD/ND)*ND (@T0)[f]
	Dodecane (DD)	40	3	fit (DD/ND*ND (@T0)[f]

ACPD
11, 9887–9957, 2011

Table A3. Continued.

Class	Species/ Parameter	Mixing Ratio	Model Input Designator	Source
Alkenes	Ethene	11 000	1	T0-Blake
	Propene	3000	1	T0-Blake
	1,3-Butadiene	230	1	T0-Blake
	1-Butene	1100	1	T0-Blake
	i-Butene	500	2	T0-Blake
	cis-2-Butene	400	1	T0-Blake
	trans-2-Butene	420	1	T0-Blake
	1-Pentene	240	2	T0-Blake
	2-Methyl-1-Butene	1	3	Estimate
	2-Methyl-2-Butene	700	2	T0-Apel
	3-Methyl-1-Butene	120	2	T0-Apel[e]
	cis-2-Pentene	210	2	T0-Blake
	Isoprene	180	1	T0-Blake
	trans-2-Pentene	410	2	T0-Blake
	1-Hexene	200	3	fit of alkenes vs. #C[f]
	2,3-Dimethylbut-2-ene	200	3	fit of alkenes vs. #C[f]
	cis-2-Hexene	200	3	fit of alkenes vs. #C[f]
	trans-2-Hexene	200	3	fit of alkenes vs. #C[f]
Alkynes	Ethyne	12 000	1	T0-Blake
Aromatics	Benzene	1700	1	T0-Blake
	Toluene	16 000	1	T0-Blake
	Ethylbenzene	1400	1	T0-Blake
	m-Xylene	1200	1	T0-Blake
	o-Xylene	600	1	T0-Blake
	p-Xylene	430	1	T0-Blake
	Styrene	40	3	Small like 1-butanol
	1,2,3-Trimethylbenzene	350	3	Estimate
	1,2,4-Trimethylbenzene	1500	1	T0-Blake
	1,3,5-Trimethylbenzene	230	1	T0-Blake
	2-Ethyltoluene	140	1	T0-Blake
	3-Ethyltoluene	370	1	T0-Blake
	4-Ethyltoluene	200	1	T0-Blake
	i-Propylbenzene	60	1	T0-Blake
	n-Propylbenzene	190	1	T0-Blake
	3,5-Dimethyl-ethylbenzene	40	3	Small like 1-butanol
	3,5-Diethyltoluene	40	3	Small like 1-butanol
Other Species	Sulfur dioxide	2200	1	T0-Kolb
	Hydrogen peroxide	1000	1	MCMA average[d]
	Methylhydroperoxide	400	1	MCMA average[d]

ACPD
11, 9887–9957, 2011

Table A3. Continued.

Class	Species/ Parameter	Mixing Ratio	Model Input Designator	Source
Odd Nitrogen	NO_x	86 000	1	T0-Kolb
	Nitrous Acid	1450	1	T0-Kolb
	PAN	18 000	1	A/C (PAN/NO_x)*NO_x (@ T0)
	PPN	2400	3	A/C(PPN/PAN)*PAN (est@ T0)
Aldehydes	Formaldehyde	5000	1	T0-Kolb
	Acetaldehyde	6000	1	T0-Kolb
	Glyoxal	200	2	T0-Kolb
	Glyoxylic acid	50	3	Estimate
	Methylglyoxal	100	3	Estimate
	Propanal (Prpn)	2850	1	A/C (Prpn/MeOH*MeOH (@T0)
	Biacetyl	100	3	Estimate
	Butanal (Btnl)	850	3	A/C (Btnl/MeOH*MeOH (@T0)
	Methylpropanal	40	3	Ratio to Butanal
	Pentanal (Ptnl)	5	3	A/C (Ptnl/DIEK)*DIEK (@T0est)
	Hexanal (Hxnl)	200	3	A/C (Hxnl/Btnl)*Btnl (@T0 est)
	Benzaldehyde	40	3	Same as methylpropanal
Ketones	Acetone (Actn)	8400	1	T0-Kolb
	MEK	1300	1	A/C (MEK/Actn)*Actn (@ T0)
	2-Pentanone (MRPK)	800	3	A/C (MPRK/MEK)*MEK (@T0)
	3-Pentanone (DIEK)	40	3	A/C(DIEK/MPRK)*MPRK(@T0)
	Methyl isopropyl ketone (MIPK)	600	3	Estimate
	2-Hexanone (2Hxn)	10	3	A/C (2Hxn/DIEK)*DIEK(@T0 est)
	3-Hexanone	10	3	Same as 2-hexanone
	Cyclohexanone	40	3	Same as methylpropanal
	4-methyl-2-pentanone (MIBK)	40	3	Same as methylpropanal
	3,3-dimethyl-2-butanone (MTBK)	40	3	Same as methylpropanal
Alcohols	Methanol (MeOH)	28 500	1	T0-Kolb
	Ethanol (EtOH)	4000	1	A/C (EtOH/MeOH)*MeOH (@T0)
	1-Propanol	300	3	Estimate: 0.01*MeOH
	2-propanol	300	3	Estimate: 0.01*MeOH
	1-Butanol	40	3	Ratio to Butanal
	2-Butanol	40	3	Ratio to Butanal
	2-Methyl-1-Propanol	40	3	Ratio to Butanal
	2-Methyl-2-propanol	40	3	Ratio to Butanal
	3-Pentanol	40	3	Same as 1-Butanol
Ethers	MTBE	1000	2	A/C (MTBE/Btnl)*Btnl (@T0 est)

ACPD
11, 9887–9957, 2011

Table A3. Continued.

Class	Species/ Parameter	Mixing Ratio	Model Input Designator	Source
Alkyl Nitrates	Methylnitrate	5	1	0.5 A/C close in average
(ANs)	Ethylnitrate	3	1	0.5 A/C close in average
	n-Propylnitrate	2	1	0.5 A/C close in average
	i-Propylnitrate	20	1	0.5 A/C close in average
	2-Butylnitrate	20	1	0.5 A/C close in average
	2-Methyl-2-Propylnitrate	10	3	Comparison w/ other ANs
	2-Methyl-Propylnitrate	10	3	Comparison w/ other ANs
	n-Butylnitrate	3	3	Comparison w/ other ANs
	1-Pentylnitrate	10	3	Comparison w/ other ANs
	2-Methyl-2-Butylnitrate	10	3	Comparison w/ other ANs
	2-Methyl-3-Butylnitrate	10	3	Comparison w/ other ANs
	2-Methyl-Butylnitrate	10	3	Comparison w/ other ANs
	2-Pentylnitrate	10	3	0.5 A/C close in average
	3-Pentylnitrate	5	1	Comparison w/ other ANs
	neo-Pentylnitrate	1	3	Comparison w/ other ANs
	1-Hexylnitrate	10	3	Comparison w/ other ANs
	2,2-dimethyl-Butylnitrate	10	3	Comparison w/ other ANs
	2,3-dimethyl-Butylnitrate	10	3	Comparison w/ other ANs
	2-Hexylnitrate	10	3	Comparison w/ other ANs
	2-methyl-1-Pentylnitrate	3	3	Comparison w/ other ANs
	2-methyl-2-Pentylnitrate	10	3	Comparison w/ other ANs
	2-methyl-3-Pentylnitrate	10	3	Comparison w/ other ANs
	2-methyl-4-Pentylnitrate	10	3	Comparison w/ other ANs
	3,3-dimethyl-Butylnitrate	10	3	Comparison w/ other ANs
	3-Hexylnitrate	10	3	Comparison w/ other ANs
	3-methyl-1-Pentylnitrate	3	3	Comparison w/ other ANs
	3-methyl-2-Pentylnitrate	10	3	Comparison w/ other ANs
	3-methyl-3-Pentylnitrate	10	3	Comparison w/ other ANs
Meteorology	Temperature, C	19		A/C outflow average
	Pressure, mb	727		A/C outflow average
	Relative Humidity, %	21.9		A/C outflow average
	Ozone column, DU	244		A/C outflow average

[a] Twenty-four hour median of measured values at T0 site by Blake et al., UC-Irvine. [b] Twenty-four hour median of measured values at T0 site reported by Kolb et al. in the database. Some measurements are from the mobile Aerodyne sampling van while others are from non-Aerodyne investigators. [c] Average of C-130 and DC-8 aircraft (A/C) observations in outflow plume. [d] Average of C-130 and DC-8 aircraft (A/C) observations within MCMA basin. [e] Twenty-four hour average as estimated from other data by Apel et al. (2010). [f] Estimated from fit of measured values of same class of compounds versus carbon number.

ACPD
11, 9887–9957, 2011

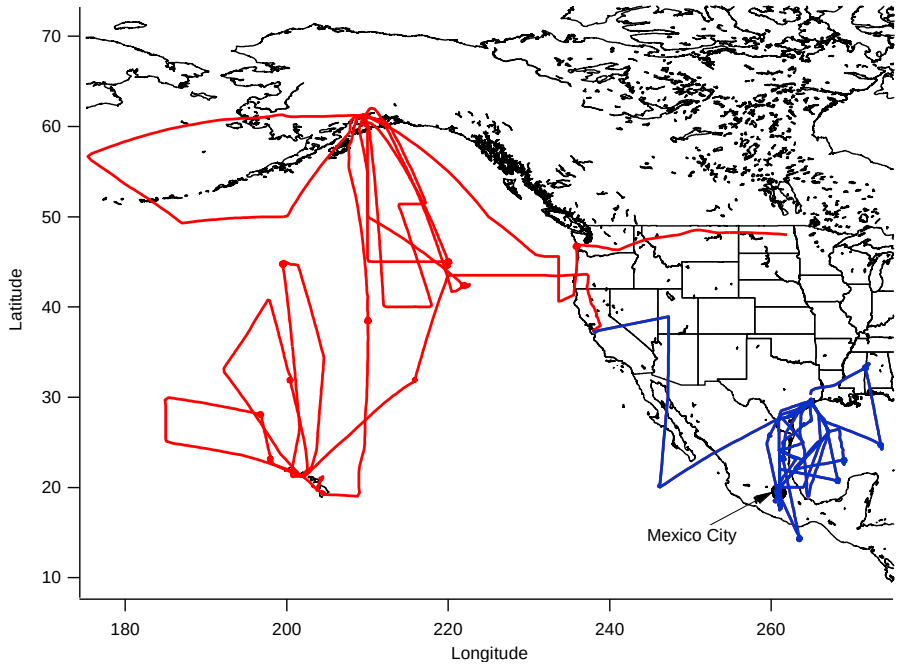

Fig. 1. DC-8 flight tracks during the INTEX-B first mission phase (blue) and second mission phase (red) on the hydrocarbon time base.

ACPD
11, 9887–9957, 2011

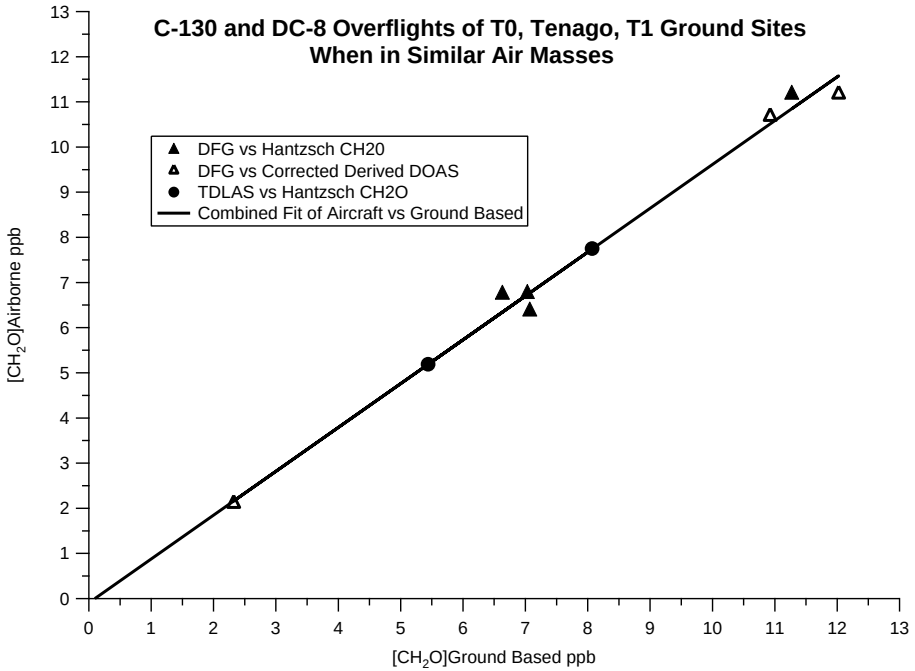

Fig. 2. Comparisons between aircraft measurements of CH_2O from the C-130 and DC-8 during over-flights with ground sites when measurements were acquired by a Hantzsch system and/or a DOAS system. The DOAS CH_2O mixing ratios were corrected by the ratio of the DOAS derived NO_2 to C-130 NO_2 measurements as discussed in the text. The DC-8 CH_2O measurements were acquired with the TDLAS system while the C-130 aircraft acquired DFG CH_2O measurements. A linear regression of the 9 points yields a slope of 0.971 ± 0.03, an intercept of -0.09 ± 0.3 ppbv and an r^2 of 0.992.

ACPD
11, 9887–9957, 2011

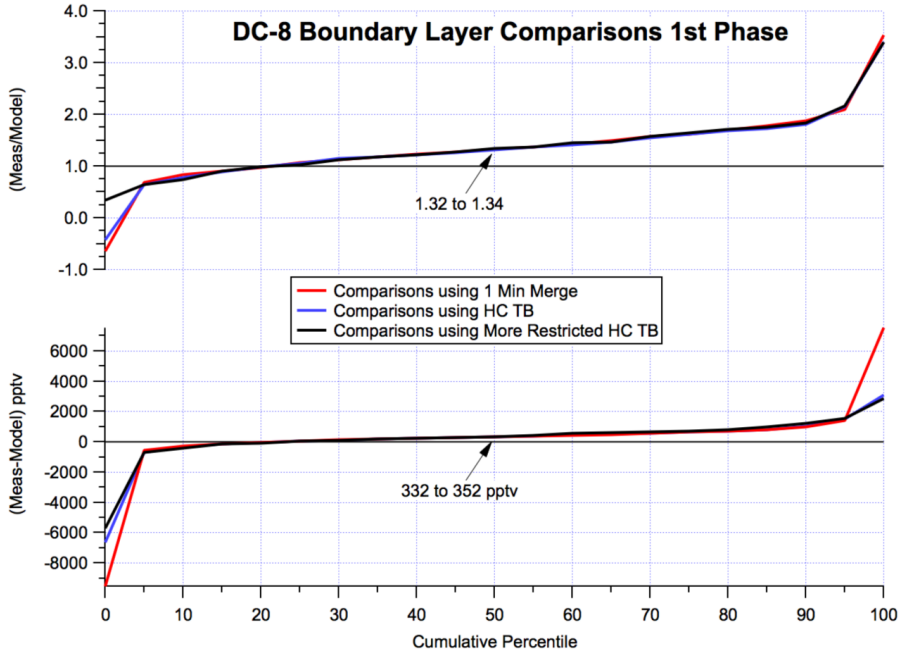

Fig. 3. Cumulative percentile measurement/model ratios and differences for DC-8 TDLAS-box model comparisons using the standard 1-minute merged data set (red line), using the hydrocarbon time base (HC TB, blue line), and using the more restricted data on the HC TB (black line), as further discussed in the text. The median ratios and differences highlighted reflect the range of values for the 3 merges. Large measurement-model discrepancies in both the ratios and differences are only observed for the lowest and highest 5% of the comparisons, indicating that comparisons are not highly dependent on the type of merge.

ACPD
11, 9887–9957, 2011

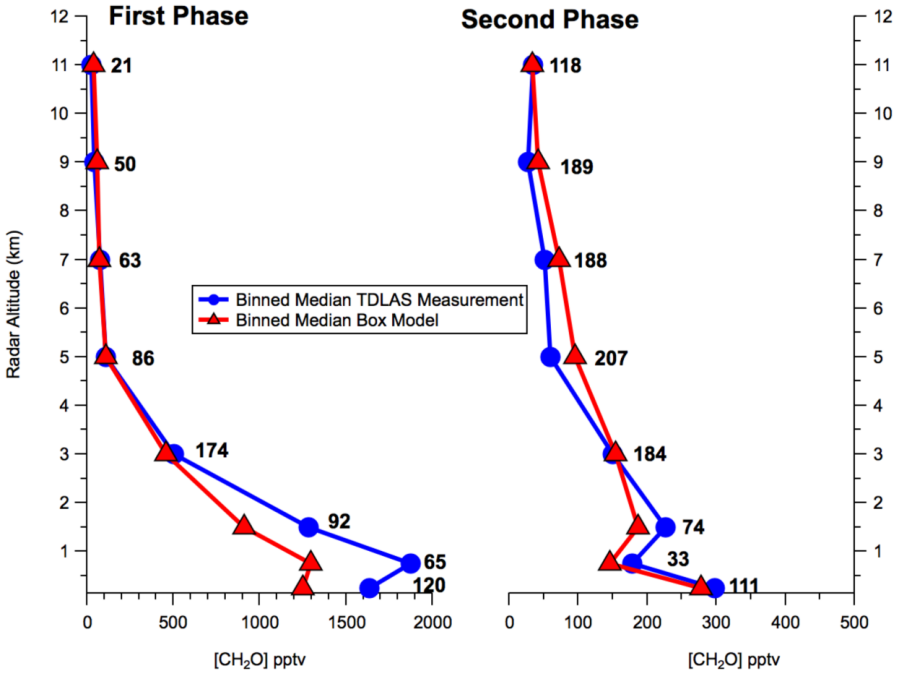

Fig. 4. Radar altitude binned medians for both mission phases. Data are averaged on hydrocarbon time base. The numbers denote the number of time coincident TDLAS measurements and model values in each bin.

ACPD
11, 9887–9957, 2011

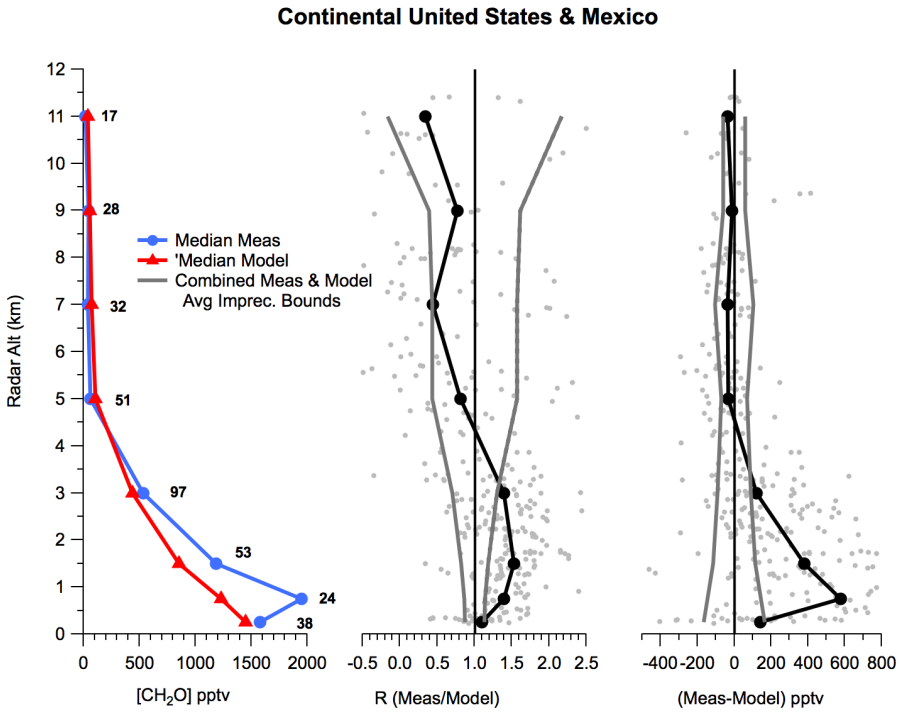

Fig. 5. Time coincident radar altitude bin TDLAS measurement (Meas)-box model (Model) comparisons on the hydrocarbon time base over the continental United States and Mexico (exclusive of Mexico City and Monterrey) during both phases of INTEX-B. The center plot shows the median point-to-point measurement/model ratios for each altitude bin (dark circles) while the right side plots the median point-to-point measurement-model differences (dark circles). Individual ratios and differences are shown by the light gray points. The solid gray lines refer to the combined average bin ratio and bin difference measurement and model uncertainties at the 2σ level using measurement imprecision and model constraint uncertainty estimates described in the text. The numbers next to each point on the left plot are the number of points in each bin.

ACPD
11, 9887–9957, 2011

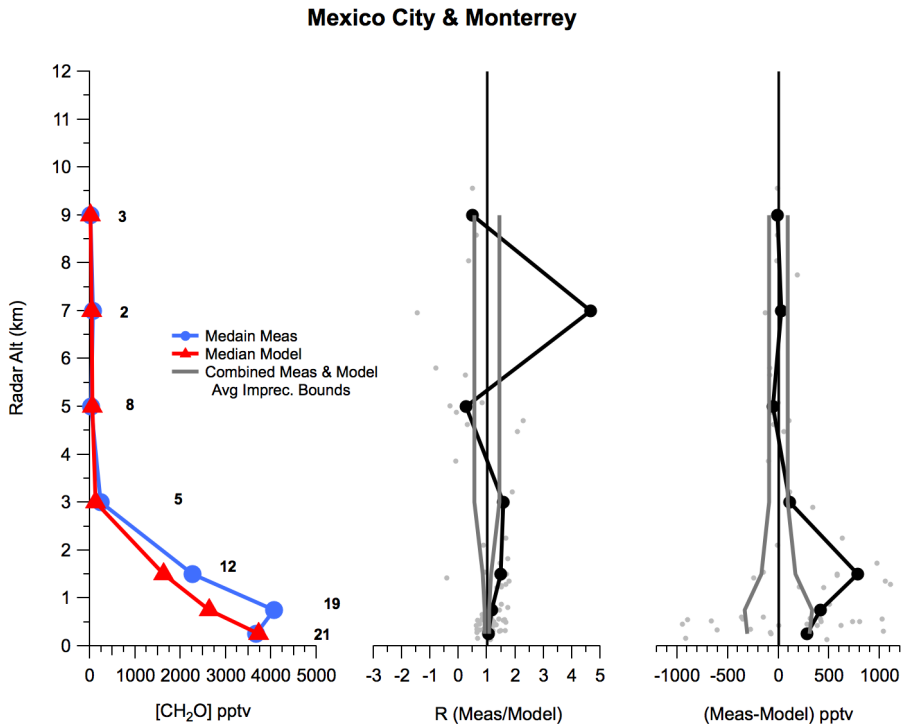

Fig. 6. Time coincident comparisons on hydrocarbon time base over Mexico City and Monterrey during the 1st phase of INTEX-B. This plot has the same format as Fig. 5. The apparent outlier ratio between 6 and 8 km is an artifact of the small number of points (2) with high measurement/model ratios but small differences. The combined imprecision limits could not be determined for the 4–6, 6–8, and 8–10 km bins and thus the values for the 2–4 km bins are repeated here for the higher altitude bins.

ACPD
11, 9887–9957, 2011

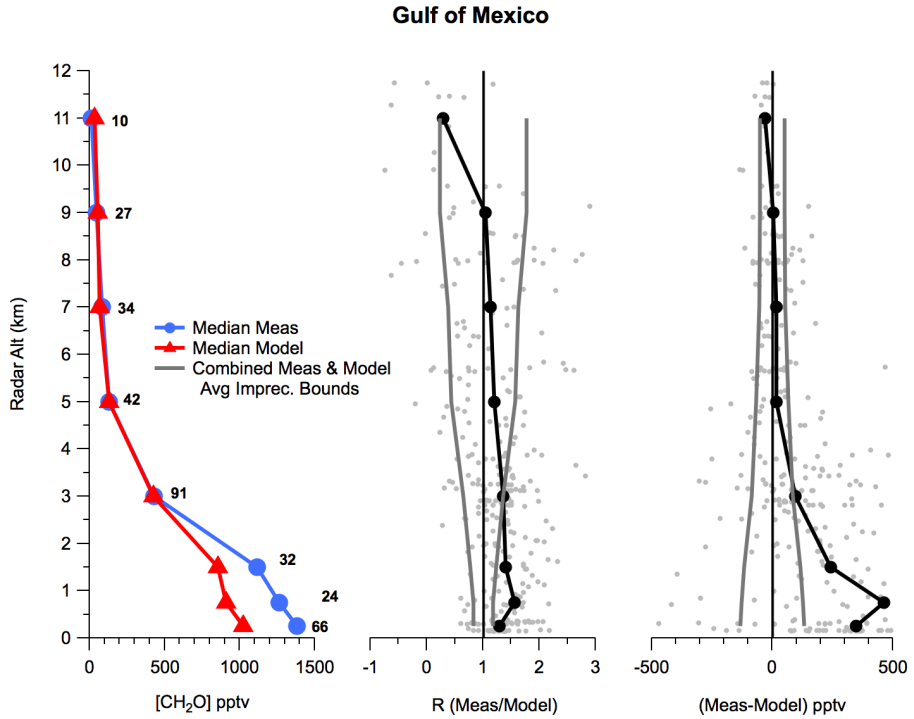

Fig. 7. Time coincident comparisons on hydrocarbon time base over the Gulf of Mexico during the 1st phase of INTEX-B. This plot has the same format as Fig. 5. The combined imprecision limits could not be determined for the 10–12 km bins (only 1 data point) and the values for the 8–10 km bins are repeated for that bin.

ACPD
11, 9887–9957, 2011

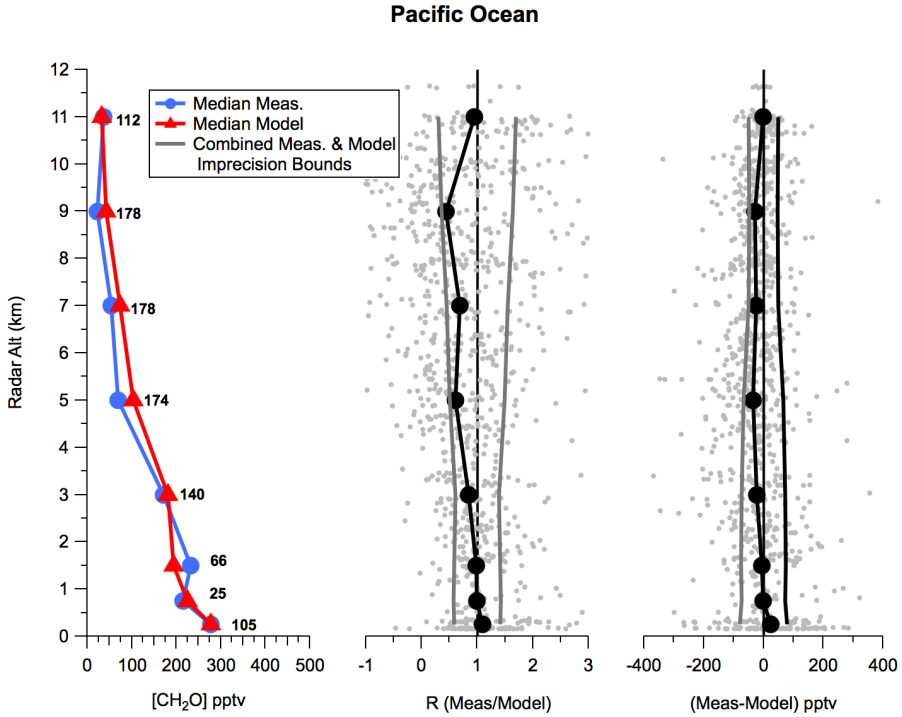

Fig. 8. Time coincident comparisons on hydrocarbon time base over the Pacific Ocean during the 2nd phase of INTEX-B. This plot has the same format as Figs. 5–7.

ACPD
11, 9887–9957, 2011

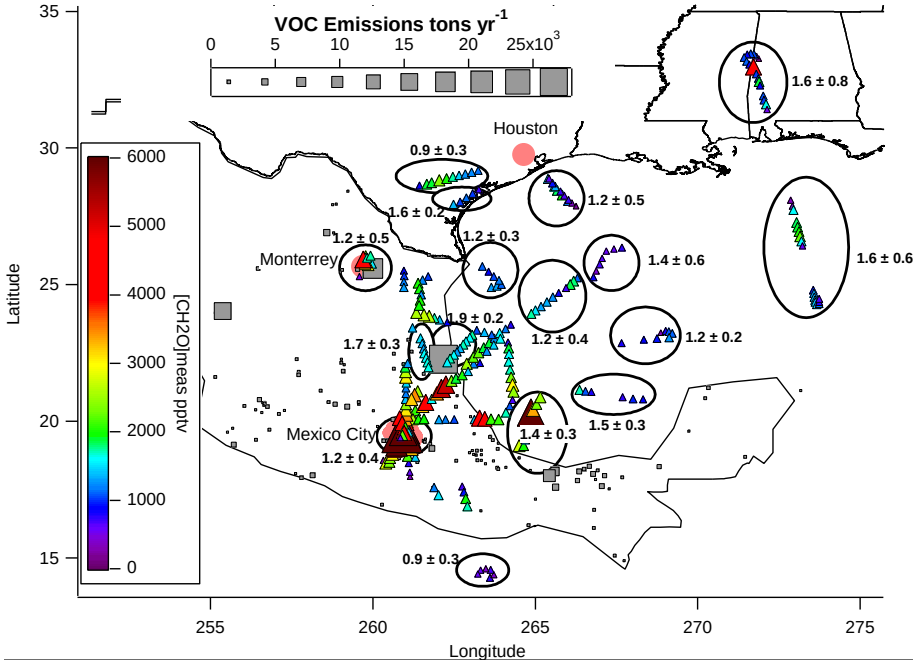

Fig. 9. Boundary layer (radar altitude <2 km) CH_2O TDLAS measurements on the hydrocarbon time base during 1st phase of INTEX-B. Mixing ratios (triangles) are colored and sized by their values. To preserve resolution the mixing ratio scale extends to only 6 ppbv. Several measurements are greater than this, including: (1) a large plume over the Gulf of Mexico (lat. = 20.2, long. = 264.9, CH_2O = 9 ppbv); (2) and numerous points over Mexico City extending up to CH_2O values of 14.6 ppbv. The filled gray squares show VOC point sources sized by their emission values in tons/year. Measurements, which are grouped into geographic flight segments (see text), are highlighted by circles. The average and standard deviation of the measurement/box model ratios for each flight segment are given adjacent to each circle.

ACPD
11, 9887–9957, 2011

Comparisons of airborne formaldehyde with box models

A. Fried et al.

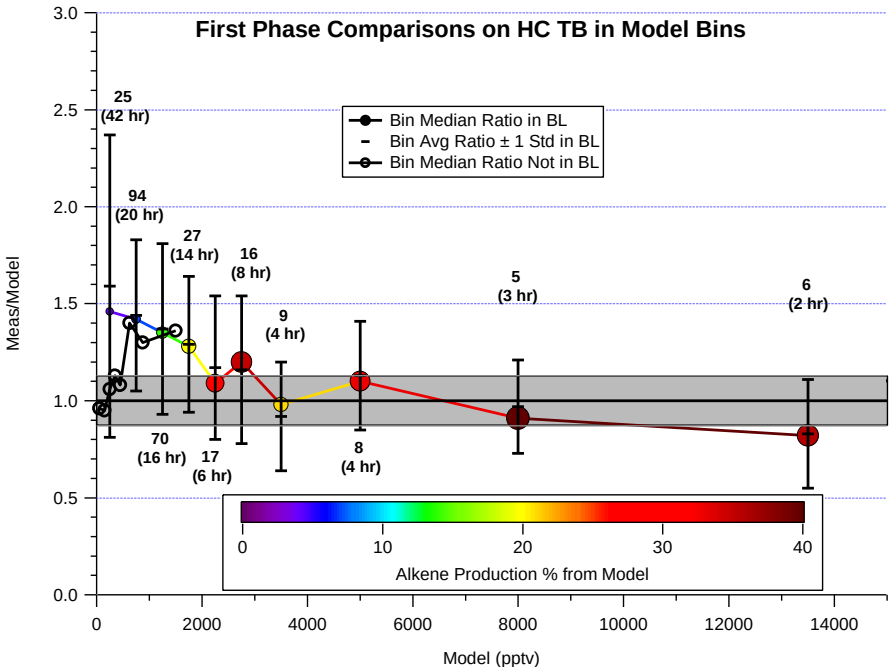

Fig. 10. TDLAS measurement/model ratios for all locations during first phase on hydrocarbon time base (HC TB) binned by model values as a function of model values. The filled colored points are in the boundary layer (BL, radar altitude <2 km) while the open black circles are outside the BL. Each BL point is colored and sized by the bin median alkene production percentage of CH_2O from the model. The number of data points in each bin is given by the top number next to each point while the bottom number represents the binned median value for the photochemical age determined from the ratio of 2-butyl nitrate to butane (see Perring et al., 2010) employing the instantaneous measured OH concentrations. The gray shaded region represents the median for the combined measurement and model 2σ uncertainty limits (±13%) in the boundary layer.

ACPD
11, 9887–9957, 2011

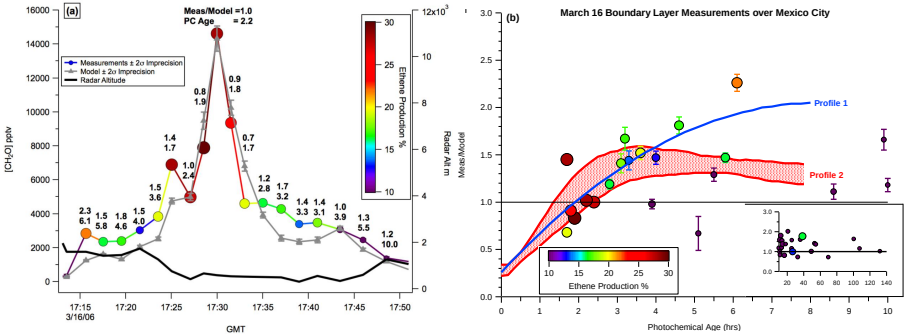

Fig. 11. (a) TDLAS measurement and model time series on the hydrocarbon time base during a flight segment in the boundary layer over the central part of Mexico City on 16 March 2006 downwind of two large VOC emitting facilities. The 2σ measurement and model uncertainties are shown with each data point by the error bars (the measurement error bars are smaller than each point size). The measurements are colored and sized by the ethene production percentage from the box model. The numbers above each comparison point represent the measurement/model ratio (upper number) and the photochemical age (PC Age) derived from the ratio of 2-butyl nitrate to butane (Bertman et al., 1995; Perring et al., 2010) employing instantaneous measured OH concentrations on the DC-8. The solid black line shows the radar altitude (right hand y-axis). **(b)** TDLAS measurement/model ratios as a function of photochemical age for the same data shown in Fig. 11a (16 March 2006), which are colored and sized by the ethene production percentage. The error bars are the combined 2σ measurement-model imprecision limits. The blue curve (Profile 1) is a 3-term polynomial regression fit of 15 data points (photochemical age $\leq$6.1 h and ethene production percentage $\geq$12%). The red profiles display the expected behavior of the box model using a Lagrangian model to simulate the time dependent behavior due to various VOC emissions in the morning (see text) in the presence of variable NO_x (0 to 25 ppbv). The ratio of the Lagrangian to box model CH_2O is plotted as a function of photochemical age. At processing times longer than ~6 h and/or lower ethene emission percentages, other sources of CH_2O become dominant (inset, which utilizes the same axes as the main plot). A linear fit of the inset points yields: intercept = 1.35 ± 0.1, slope = -0.002, r^2 of 0.02.

ACPD
11, 9887–9957, 2011

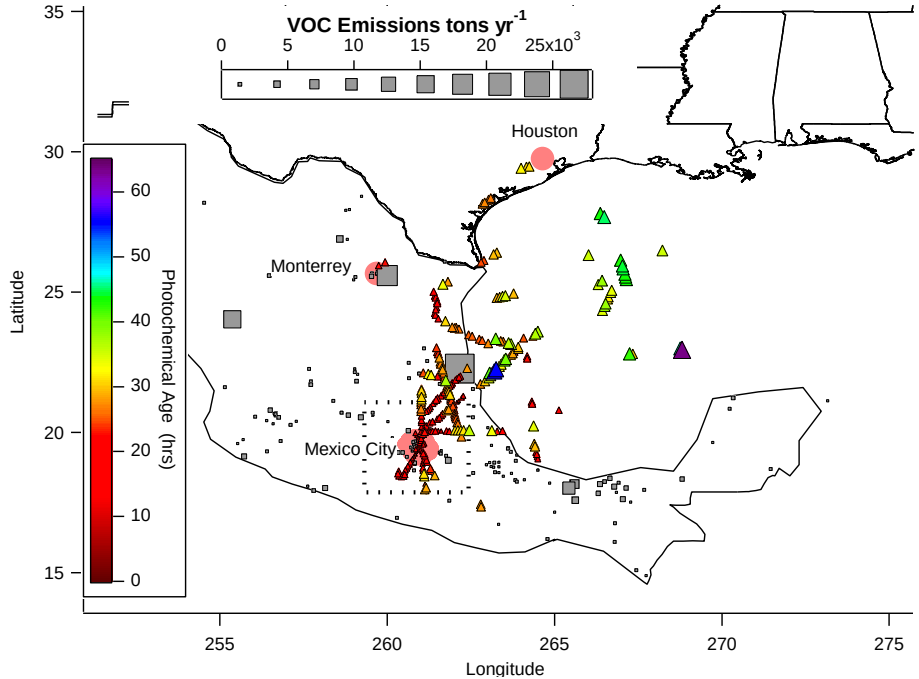

Fig. 12. Mexico City outflow events (1-min merged time base) based upon criteria discussed in text colored and sized by photochemical age from the ratio of 2-butyl nitrate to butane (Bertman et al., 1995; Perring et al., 2010). As in Fig. 9, the solid gray squares show VOC point sources sized by their emission values in tons/year. The dashed black square denotes the approximate limit for the region we define as the Mexico City area.

ACPD
11, 9887–9957, 2011

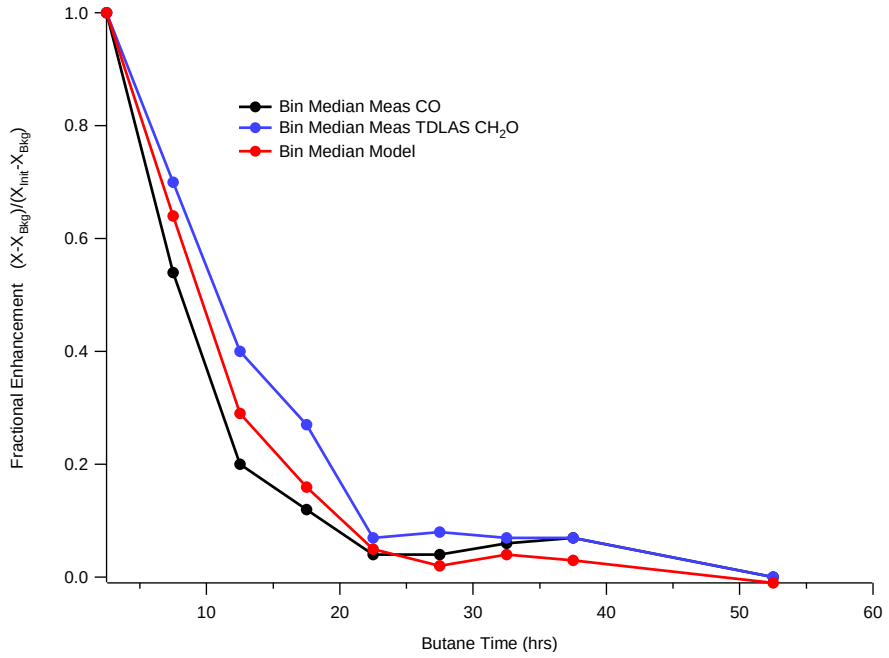

Fig. 13. Fractional enhancement for CH_2O TDLAS measurements, box model values as well as CO observations as a function of the butane time employing a constant diurnally averaged OH concentration of 3×10^6 molecules cm^{-3} based upon Perring et al. (2010). The fractional enhancements were determined from the ratio of the median bin values minus background values over median initial values over Mexico City minus background values (see text for values).

ACPD
11, 9887–9957, 2011

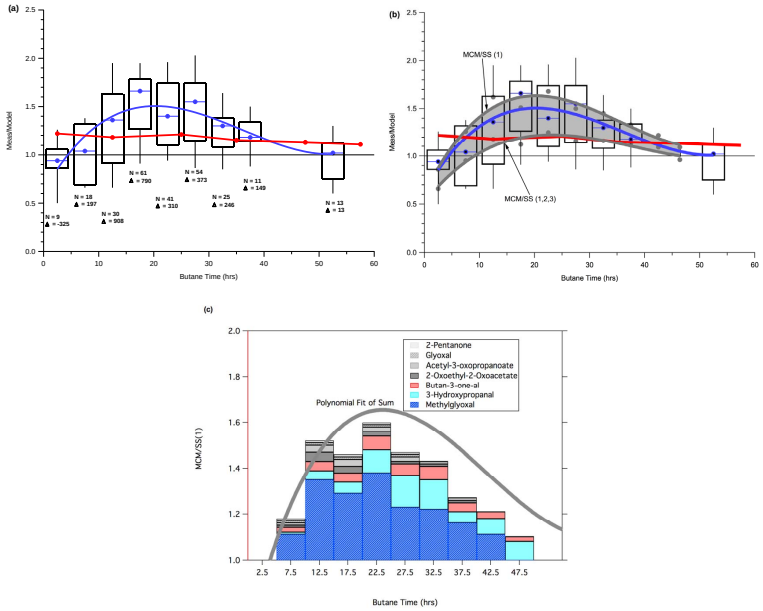

Fig. 14. **(a)** Box and whisker plot for the TDLAS measurement/model ratio for Mexico City outflow events as a function of the butane time. The boxes denote the interquartile values, the horizontal lines with blue circles are the median ratios and the whisker represent 10 and 90 percentiles values. The blue solid profile is an empirical 4-term polynomial fit of the median TDLAS ratios to the butane time while the red line with points represents a proxy for this ratio based upon the ratio of Lagrangian-to-steady state predictions (see manuscript for details). The numbers below each whisker plot denote the number of TDLAS comparisons in that bin (top number) and the median point-by-point measurement-model differences (Δ) in pptv are denoted by the lower numbers. **(b)** The same plot as **(a)** with the addition of two Master Chemical Mechanism (MCM) runs as additional proxies for the measurement/model ratio. The upper gray profile is a 4-term polynomial fit of the upper gray points, which plot the median ratio of the MCM run to steady-state, with the steady-state calculations using model input designator **1** discussed in Table A3 of the Appendix. The lower gray profile is the polynomial fit of the lower gray points, which include all species (species **1, 2, 3** in Table A3) in the steady-state calculation (revealing the impact of differences from steady-state only). The difference between the two gray profiles represents formation of CH_2O from unmeasured species and from unmeasured multi-generation species. **(c)**The MCM output showing the 7 major species responsible for producing the CH_2O not accounted for in the steady-state model as a function of the 5-h binned butane time (the bin mid time is plotted here). These species are multiply-substituted second-and higher-generational products of species for which the MCM was initialized. As in the previous plot, the solid gray line is a polynomial fit for the ratio due to all species.

ACPD
11, 9887–9957, 2011